**OAK RIDGE
NATIONAL LABORATORY**

MANAGED BY UT-BATTELLE
FOR THE DEPARTMENT OF ENERGY

Engineering Science & Technology Division

Control of Surface Mounted Permanent Magnet Motors with Special Application to Motors with Fractional-Slot Concentrated Windings

Niranjan Patil
University of Tennessee

Dr. J. S. Lawler
University of Tennessee

Dr. John McKeever
Oak Ridge National Laboratory

UT-BATTELLE

ORNL-27 (4-00)

1

TABLE CONTENTS

LIST OF FIGURES

LIST OF TABLES

ACRONYMS

CPA	conventional phase advance
CPSR	constant power speed ratio
dc	direct current
emf	electromotive force
FFT	fast fourier transform
FPGA	field programmable gate array
FSCW	fractional-slot concentrated windings
HEV	hybrid electric vehicle
ORNL	Oak Ridge National Laboratory
PM	permanent magnet
PMSM	permanent magnet synchronous motor
PWM	pulse width modulation
rms	root-mean square
rpm	revolutions per minute
SPM	surface-mounted PM
SSPB	sensorless simple parameter based
UWM	University of Wisconsin at Madison
VSI	voltage-source inverter

EXECUTIVE SUMMARY

A 30 pole, 6 kW, and 6000 maximum revolutions per minute (rpm) prototype of the permanent magnet synchronous motor (PMSM) with fractional-slot concentrated windings (FSCW) has been designed, built, and tested at the University of Wisconsin at Madison (UWM). This machine has significantly more inductance than that of regular PMSMs. The prototype was delivered in April 2006 to the Oak Ridge National Laboratory (ORNL) for testing and development of a controller that will achieve maximum efficiency. In advance of the test/control development effort, ORNL has used the PMSM models developed over a number of previous studies to study how steady state performance of high inductance PMSM machines relates to control issues. This report documents the results of this research.

The amount of inductance that enables the motor to achieve infinite constant power speed ratio (CPSR) is given by

$$L_\infty = \frac{E_b}{\Omega_b I_R},$$

where E_b is the root-mean square (rms) magnitude of the line-to-neutral back-electromotive force (emf) at base speed,

Ω_b is the base speed in electrical radians per second, and

I_R is the rms current rating of the motor windings.

The prototype machine that was delivered to ORNL has about 1.5 times as much inductance as a typical PMSM with distributed integral slot windings. The inventors of the FSCW method, who designed the prototype machine, remarked that they were "too successful" in incorporating inductance into their machine and that steps would be taken to modify the design methodology to reduce the inductance to the optimum value. This study shows a significant advantage of having the higher inductance rather than the optimal value because it enables the motor to develop the required power at lower current thereby reducing motor and inverter losses and improving efficiency. The main problem found with high inductance machines driven by a conventional phase advance (CPA) method is that the motor current at high speed depends solely on machine parameters and is virtually independent of the load level and the direct current (dc) supply voltage. Thus, the motor current is virtually the same at no load as at full load resulting in poor efficiency at less than full load conditions.

While an inductance higher than the value cited above is warranted, it still does not ensure that the motor current is proportional to load; consequently, the problem of low efficiency at high speed and partial load is not resolved but is only mitigated.

A common definition of "base speed" is the speed at which the voltage applied to the motor armature is equal to the magnitude of the back-emf. The results in this study indicate that the dc supply voltage should be adequate to drive rated current into the motor winding at the specified base speed. At a minimum this requires sufficient voltage to overcome not only the back-emf but also the voltage drop across the internal impedance of the machine. For a high inductance PMSM, the internal impedance at base speed can be considerable and substantial additional voltage is required to overcome the internal voltage drop. It is further shown that even more voltage than the minimum required for injecting rated current at base speed can be beneficial by allowing the required power to be developed at lower current, which reduces losses in the motor and inverter components. Further, it is shown that the current is

minimized at a unique speed; consequently, there may be room for optimization if the drive spends a substantial amount of its operating life at a certain speed (for example 60 mph).

In this study, fundamental frequency phasor models are developed for a synchronous PMSM and the control systems that drive them is CPA. The models were compared with detailed simulations to show their validity. The result was used to design a traction drive control system with optimized efficiency to drive the fractional-slot motor with concentrated windings. The goal is to meet or exceed the FreedomCAR inverter cost and performance targets.

1.0 INTRODUCTION

A 30-pole, 6-kW prototype of a fractional-slot permanent magnet synchronous motor (PMSM) design has been developed to operate at a maximum speed of 6000 rpm [1,2]. This machine has significantly more inductance than regular PMSMs with distributed windings. The prototype was delivered in April 2006 to the Oak Ridge National Laboratory (ORNL) for testing and development of a suitable controller. To prepare for this test/control development effort, ORNL used PMSM models developed over a number of previous studies to preview the control issues that arise when a dynamic controller drives a high inductance PMSM machine during steady state performance evaluations. The detailed steady state model developed includes all motor and inverter loss mechanisms and was useful for assessing the performance of the dynamic controller before it was put into operation. This report documents the results of tests demonstrating the effectiveness of ORNL's simple low-cost control scheme during characterization of the fractional-slot concentrated windings (FSCW) PMSM motor. The control scheme is simple because only the supply voltage magnitude and the phase angle between the back-electromotive force (emf) and the supply voltage is controlled. It is low-cost because it requires no current or phase voltage sensors.

1.1   BACKGROUND AND SUMMARY

The late Peter Wood, a well known figure in the field of power electronics, once characterized the nature of problem solving in power electronics as akin to eliminating bulges in a bag of water. If a particular bulge in the bag represents a problem and depressing the bulge represents a solution then one needs to be aware that while the target bulge may be gone, another bulge may have surfaced some where else on the bag. A major conclusion of this study is that while a method of incorporating high winding inductance in PMSM design may solve the constant power speed ratio (CPSR) problem, it can make it difficult to meet efficiency objectives at higher speeds especially under less than full load conditions. Since a traction drive may spend considerable operating time near one half of the maximum speed, and at approximately one quarter of the full load, the lack of high efficiency under such conditions may be a problem.

Another significant issue regarding high inductance PMSMs uncovered in this study involves the amount of inductance required to meet CPSR requirements. It is generally believed that there is an "optimum value" for field weakening that is given by

$$L_\infty = \frac{E_b}{\Omega_b I_R} \tag{1}$$

where E_b is the root-mean square (rms) magnitude of the line-to-neutral back-emf at base speed, Ω_b is the base speed in electrical radians per second, and I_R is the rms current rating of the motor windings. The prototype machine that was delivered to ORNL has about $1.5 L_\infty$. The inventors of the FSCW method, who designed the 6-kW prototype machine, remarked that they were "too successful" in incorporating inductance into their machine and that steps would be taken to modify the design methodology to reduce the inductance to the optimum value. This study will show a significant advantage of having the higher inductance rather than the "optimal" value. Specifically, it is shown that the higher inductance enables the motor to develop the required power at lower current thereby reducing motor and inverter losses and improving efficiency. While an inductance higher than the value cited above is warranted, it still does not make the motor current proportional to load. Consequently, the problem of low efficiency at high speed and less than full load is not resolved, it is only mitigated.

A final point uncovered in this study concerns the direct current (dc) supply voltage that provides the underlying source for the traction drive. A common definition of "base speed" is the speed at which the

1

voltage applied to the motor armature is equal to the magnitude of the back-emf. The results in this study indicate that the dc supply voltage must be adequate to drive rated current into the motor winding at the specified base speed. At a minimum, this requires sufficient voltage to overcome not only the back-emf but also the voltage drop across the internal impedance of the machine. For a high inductance PMSM, the internal impedance at base speed can be considerable and substantial additional voltage is required to overcome the internal voltage drop. It is further shown that even more voltage than the minimum required for injecting rated current at base speed can be beneficial. In particular, this allows the required power to be developed at lower current with reduced copper losses in the motor and inverter components. Further, it is shown that the current is minimized at a unique speed which varies with voltage; consequently there may be room for optimization. For example, if the drive spends a substantial amount of its operating life near half of maximum speed, then it can be desirable to choose a dc supply voltage which causes the motor current to achieve its minimum value at half of full speed.

The line-neutral back-emf voltage constant, K_v, in Table 1 is the slope of the no-load rms back-emf averaged over the three phases and plotted against motor speed.

Table 1. Parameters of the 6-kW surface-mounted PM (SPM) FSCW motor

Parameter		Rated or measured values
Number of poles		30
Base speed		900 rpm
Top speed		6000 rpm
CPSR requirement		6.667:1
Back-emf magnitude at base speed, Eb (rms volts per phase)		49.45 @ 900 rpm
Voltage constant, Kv (rms volts per elec. rad/sec)		0.03497
Rated power		6 kW
Rated torque		63.66 Nm
Rated rms current		40.44 A
Resistance per phase		76 mΩ
Inductance per phase		1.3 mH

1.2. ORGANIZATION OF THE REPORT

Analysis of PMSM driven by a conventional phase advance (CPA) method is described in Chapter 2. Chapter 3 has details about experimental setup. Results and graphs are in Chapter 4 and finally, the conclusion is in Chapter 5.

2.0 ANALYSIS OF THE PMSM WHEN DRIVEN BY CPA

Figure 1 shows a schematic of the three-phase PMSM driven by a voltage-source inverter (VSI) as used by the CPA method. The figure also defines some of the parameters and notation used in this discussion. The resistors R and R_{rot} represent the copper losses and the speed sensitive rotational losses respectively. The value of R_{rot} can be calculated for any given speed using the least-squares fit of the rms back-emf and the least squares-fit of rotational no-load losses, both obtained from measured data. At relative speed n, the value of $R_{rot}(n)$ is calculated as

$$R_{rot}(n) = \frac{3(nE_b)^2}{P_{rot}(n)} \ .$$
(2)
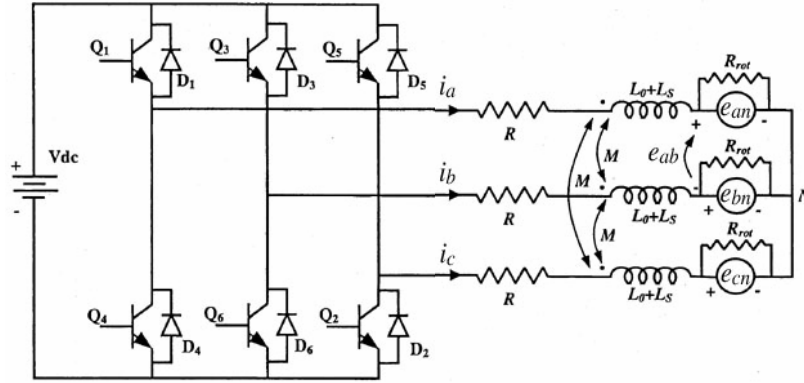
Fig. 1. Motor/inverter schematic for PMSM driven by CPA.

p = number of poles,
N = actual mechanical rotor speed in revolutions per minute (rpm),
N_b = mechanical base speed in rpm,
n = relative speed = $\dfrac{N}{N_b}$,
Ω_b = base speed in electrical radians/sec,
  = $\dfrac{p}{2} \cdot \dfrac{2\pi N_b}{60}$,
Ω = actual rotor speed in electrical radians/sec,
  = $n\Omega_b$,
E_b = rms magnitude of the phase-to-neutral emf at base speed,
I_R = rated rms motor current,
P_R = rated output power = $3E_b I_R$,
L_s = self inductance per phase,
L_o = leakage inductance per phase,
M = mutual inductance,
L = equivalent inductance per phase = $L_o + L_s + M$,
R = winding resistance per phase,
v_{an} = applied phase A to neutral voltage,

3

e_{an} = phase A to neutral back-emf, and
e_{ab} = phase A to phase B (line-to-line) back-emf.

The detailed technical assessment of the motor includes the evaluation of losses, not only in the motor but also in the inverter. The main focus in Section 2 is on CPSR performance and current magnitude control and the discussion is greatly simplified by neglecting the losses. Unless otherwise specified, the discussion in the remainder of this section and the next assumes that the winding resistance, R, is zero and the rotational loss resistance, R_{rot}, is infinite.

The transistors in the inverter of Fig. 1 are typically controlled by sinusoidal pulse width modulation (PWM) which uses a triangular carrier wave and three sinusoidal reference waves to decide the switching pattern. A detailed PSPICE simulator is available to analyze the performance of the PMSM as displayed in Fig. 1 and controlled by PWM when operating at constant speed. Since the objective here is to focus on CPSR, efficiency, and steady state control the details of PWM control are intentionally omitted and a simplified per-phase fundamental frequency model is developed. Such a model is shown in Fig. 2 which is a phasor model of the motor drive at a selectable but constant speed.

ORNL 2002-03422/jcn
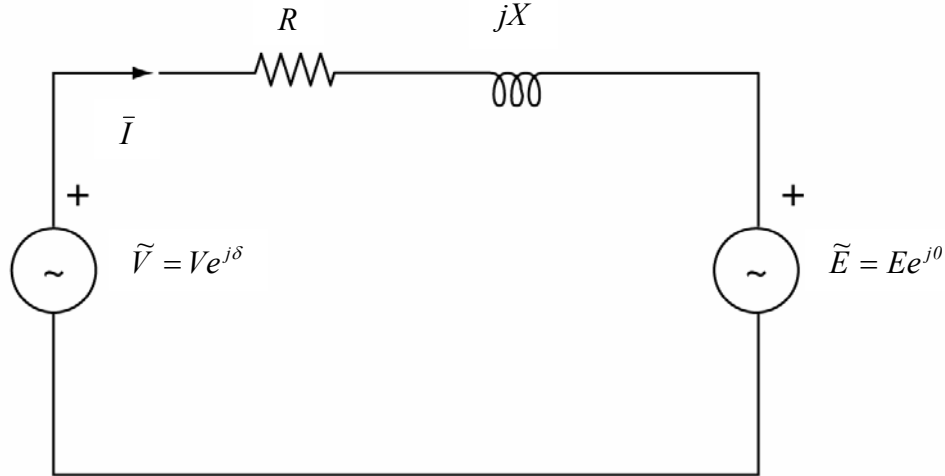
Fig. 2. Fundamental frequency model of one phase of a PMSM.

In the per-phase model of Fig. 2, the phasor $\tilde{V}$ represents the fundamental frequency line-to-neutral voltage applied to the motor by the inverter. V is the rms magnitude and δ is the inverter lead angle, which is the angle by which the voltage leads the back-emf. Phasor $\tilde{E}$ represents the phase-to-neutral motor back-emf and is chosen as the reference phasor, such that its phase angle is zero. The magnitude of the back-emf is linear in motor speed and the voltage constant, K_v, has units of rms volts per electrical radian per second. Thus, the rms value of the back-emf at any speed is given by

4

$$E = K_v \Omega$$

$$= \frac{\Omega}{\Omega_b} K_v \Omega_b \quad , \tag{3}$$

$$= n E_b$$

where E_b is the rms magnitude of the line-to-neutral back-emf at base speed and n is relative speed. Similarly, the motor reactance can be expressed as

$$X = \Omega L$$

$$= \frac{\Omega}{\Omega_b} \Omega_b L \quad , \tag{4}$$

$$= n X_b$$

where X_b is the reactance at base speed.

2.1 BASE SPEED DEFINED

We should distinguish between "base speed" and "true base speed." Base speed is the highest speed at which rated torque <u>is required</u>, and the power developed at this speed is the rated power of the motor drive. True base speed is the highest speed at which rated torque <u>can be developed</u>. The true base speed is exactly the same as base speed when the dc supply voltage is selected as the minimum value that permits rated torque to be developed at the base speed and is given by

$$V_{dc-\min} = \frac{\pi}{\sqrt{2}} \sqrt{E_b^2 + \left(X_b I_R \right)^2} \quad . \tag{5}$$

This expression assumes that the PWM control will be in full over-modulation when developing rated torque at base speed. Note that Eq. (5) insures that sufficient dc supply voltage is provided so that at base speed the driving voltage is sufficient to overcome the back-emf voltage <u>and</u> the internal impedance of the motor while supplying the rated current to the windings. For this motor having inductance of $1300\,\mu H$, the required dc supply voltage is 198.3 V. If the dc supply voltage is less than $V_{dc-\min}$, it will not be possible to develop rated torque at the specified base speed and the true base speed will be less than the specified value. If the dc supply voltage is larger than $V_{dc-\min}$, then the true base speed is larger than the specified value. Letting the true base speed be denoted as n_{bt} we have

$$n_{bt} = \frac{V_{dc}}{V_{dc-\min}} \cdot n_b \quad . \tag{6}$$

When a dc supply larger than the minimum is used, the rated torque <u>can</u> be developed at a speed higher than base speed resulting in greater power conversion capability; however, the drive control can be configured to preclude using this extra capability restricting the maximum torque above base speed. Even though control may be used to constrain the torque speed envelope, the addition of surplus dc supply

voltage may allow reduced current magnitude at high speed, thereby reducing inverter and motor copper losses and improving efficiency. This possibility is discussed further in Section 2.1.

2.2 BELOW BASE SPEED

Up to base speed, the magnitude of the applied phase voltage, V, and the lead angle, δ, can be adjusted allowing the motor current phasor to be in phase with the back-emf. This maximizes the torque produced per amp. Voltage magnitude, V, and lead angle, δ, required to support any relative speed below base speed for which $n \leq 1$ is

$$
\begin{aligned}
\bar{V} &= nE_b + jnIX_b \\
&= \sqrt{\left(nE_b\right)^2 + \left(nIX_b\right)^2} \angle \tan^{-1}\left(\frac{nIX_b}{nE_b}\right) \\
&= n\sqrt{E_b^2 + \left(X_bI\right)^2} \angle \tan^{-1}\left(\frac{IX_b}{E_b}\right) \\
&= V \angle \delta
\end{aligned}
\qquad (7a)
$$

From Fig. 2 and Eq. (7a), the rms current, I, is

$$
\tilde{I} = \frac{V \angle \delta - nE_b \angle 0}{jnX_b} = \frac{V \sin\delta}{nX_b} + j\frac{\left(nE_b - V \cos\delta\right)}{nX_b} \quad .
\qquad (7b)
$$

Since $V\cos\delta = nE_b$ by the first and fourth lines of Eq. (7a), it follows that I only has a real component, which is in phase with the back-emf. The rms magnitude of $\tilde{V}$ increases with speed as the modulation index increases from 0 to $4/\pi$ and the voltage vector extends from the origin at constant δ until it reaches its maximum value, which is limited by the available dc supply voltage. Assuming that the dc supply voltage is the minimum value and that full over-modulation is allowed, the maximum phase voltage magnitude is obtained at base speed where $n = 1$ and rated rms motor current is $I = I_R$, then

$$
V_{\max} = \sqrt{\left(E_b\right)^2 + (I_R X_b)^2} = \sqrt{\left(E_b\right)^2 + (I_R \Omega_b L)^2} \quad .
\qquad (8)
$$

Similarly, the lead angle δ at base speed for rated current is given by the third and fourth lines of Eq. (7a) as

$$
\delta = \tan^{-1}\left(\frac{I_R X_b}{E_b}\right) \quad .
\qquad (9)
$$

The power developed at base speed and rated current is the rated power of the motor and since the current is in phase with the back-emf we have

$$
P_R = 3E_b I_R \quad .
\qquad (10)
$$

6

2.3   ABOVE BASE SPEED

Let us now restrict our attention to operation above base speed such that $n > 1$ and $V = V_{max}$. Neglecting the armature resistance, the phasor current of the motor is

$$\tilde{I} = \frac{V_{max}}{nX_b}\sin\delta + j\left[\frac{E_b}{X_b} - \frac{V_{max}}{nX_b}\cos\delta\right],$$

$$= I_r + jI_x$$

(11)

where I_r is the component of current in phase with the back-emf and produces useful torque. This component is like the q-axis current in the d-q model and can be referred to as the torque producing component. I_x is the component of current that is orthogonal to the back-emf and results in no net torque production. This component is like the d-axis current in the d-q model and can be referred to as the field weakening current. The total motor current has rms magnitude

$$I = \sqrt{I_r^2 + I_x^2}$$

$$= \frac{\sqrt{V_{max}^2 - n2V_{max}E_b\cos\delta + n^2E_b^2}}{nX_b}.$$

(12)

The total power injected into the motor by the inverter is

$$P_{in} = 3\,\mathrm{Re}(\tilde{V}\tilde{I}^*) = \frac{3V_{max}E_b}{X_b}\sin\delta,$$

(13)

while the total power converted by the motor is

$$P_m = 3\,\mathrm{Re}(\tilde{E}\tilde{I}^*) = \frac{3V_{max}E_b}{X_b}\sin\delta$$

$$= P_{max}\sin\delta$$

(14)

where

$$P_{max} = 3\frac{V_{max}E_b}{X_b}$$

(15)

is the maximum power that can possibly be converted, which corresponds to the lead angle being 90°. Since we have neglected the winding resistance, P_{in} equals P_m and the common value is

$$P_m = P_{in} = \frac{3V_{max}E_b}{X_b}\sin\delta$$

$$= P_{max}\sin\delta \qquad (16)$$

This expression shows that it is easy to control the motor to deliver rated power above base speed. All that is necessary is that the inverter lead angle, δ, be held fixed at that value which causes P_m in Eq. (15) to be equal to the rated value, P_R, given in Eq. (10); that is

$$\delta = \sin^{-1}\left(\frac{X_b P_R}{3V_{max}E_b}\right)$$

$$= \cos^{-1}\left(\frac{E_b}{V_{max}}\right) \qquad (17)$$

While constant lead angle control allows the PMSM to operate at constant power above base speed, it is not a certainty that doing so results in operating within the rated current. The critical factor is the motor inductance as shown below.

Equation (12) gives the rms motor current, I, when operating at any speed above base speed. Using lead angle, δ, from Eq. (17) so that rated power is produced, we require that the rms current in Eq. (12) be no greater than the rated value I_R; that is

$$I = \frac{\sqrt{V_{max}^2 - 2nV_{max}E_b\cos\delta + n^2 E_b^2}}{nX_b}$$

$$= \frac{\sqrt{V_{max}^2 + n(n-2)E_b^2}}{n\Omega_b L} \qquad (18)$$

$$\leq I_R$$

There is a well defined speed at which the current magnitude is minimal. Setting the derivative of Eq. (18) with respect to relative speed, n, equal to zero and solving for this speed yields

$$n_{min} = \frac{V_{max}}{E_b\cos\delta} \qquad (19)$$

With this value of n substituted into Eq. (18), the minimum current is found to be

$$I_{min} = \frac{P}{3V_{max}}. \qquad (20)$$

Note that this minimum current magnitude is independent of motor parameters and depends linearly on the developed power and inversely on the maximum fundamental inverter voltage. Since V_{max} can be increased by raising the dc supply voltage, there may be a reduction in motor and inverter losses when

V_{dc} is increased above the minimum level required to sustain rated power at base speed. It can be shown that for speeds less than n_{min}, the <u>inverter</u> power factor is lagging; while for speeds above n_{min}, the <u>inverter</u> power factor is leading. Thus, the inverter operates at the optimum unity power factor condition at only one speed, namely n_{min}.

Observe from Eqs. (11) and (18) that as the speed approaches infinity, the motor current magnitude approaches a limiting value given by

$$\lim_{n \to \infty} I_r = \lim_{n \to \infty} \frac{V_{max}}{nX_b} \sin \delta = 0$$

$$\lim_{n \to \infty} I_x = \lim_{n \to \infty} \left(\frac{E_b}{X_b} - \frac{V_{max}}{nX_b} \cos \delta \right) = \frac{E_b}{X_b} = \frac{E_b}{\Omega_b L}$$

$$\lim_{n \to \infty} I = \lim_{n \to \infty} \frac{\sqrt{V_{max}^2 + n(n-2)E_b^2}}{nX_b} = \frac{E_b}{X_b} = \frac{E_b}{\Omega_b L} = I_{CH}$$

(21)

2.4 "OPTIMAL" INDUCTANCE FOR FIELD WEAKENING

The limiting rms current magnitude in Eq. (21) is called the "characteristic current" [3] denoted as I_{CH}. The characteristic current in Eq. (21) is larger than the minimum current in Eq. (20). For this motor, the value of the characteristic current is 26.9 A, which is less than the rated current 40.44 A. Note that the characteristic current depends only on motor parameters E_b, Ω_b, and L and is independent of motor load and dc supply voltage. Also note that at high speeds the torque producing current, I_r, approaches zero so that the limiting current at high speed is solely due to field weakening current, I_x. This result has a positive implication for being able to operate over a wide CPSR while remaining within the motor current rating. Unfortunately, there is also an adverse implication towards efficiency when operating at high speed and partial load. The impact on efficiency is considered later. At the moment, we consider the positive impact on CPSR when the machine inductance is sufficiently large.

If we require the limiting rms current in Eq. (21), which is the characteristic current, to be less than or equal to the rated current, I_R, then we have an inductance requirement that yields an infinite CPSR which is

$$L_\infty = \frac{E_b}{\Omega_b I_R}$$

(22)

This inductance value is sometimes cited as the "optimal" value for field weakening [3]. Any PMSM having an inductance with the value in Eq. (22) or higher, will have an infinite CPSR.

2.5 THE PROBLEM WITH DEFINING BASE SPEED AS THE SPEED WHERE $V_{MAX} = E_B$

Applying Eq. (22) to the parameters of the example motor in Table 1, where $E_b = 49.45\,V$, $\Omega_b = 1413.7$ electrical radians/sec, and $I_r = 40.44$ A, leads to an inductance of 1300 μH, which exceeds the "optimal" value by a factor of 1.55. The assertion that the inductance in

9

Eq. (22) is optimal is tied to a notion of base speed where the voltage magnitude applied by the inverter is maximum and is exactly equal to the magnitude of the back-emf. When this is the case,

$$V_{\max} = E_b \Rightarrow V_{dc} = \frac{\pi E_b}{\sqrt{2}} \qquad (23)$$

and from Eq. (15)

$$P_{\max} = \frac{3V_{\max}E_b}{\Omega_b L_\infty} \equiv P_R \quad . \qquad (24)$$

In this case, the rated power is the maximum power that can be developed. If $V_{\max}$ is restricted to the value, E_b, then any machine with an inductance larger than L_∞ would not be able to develop rated power at high speed. Although not shown here, when the dc supply is restricted as in Eq. (23), a motor with the "optimal inductance" would be able to develop rated power at high speed, but not at base speed. A motor with an inductance greater than L_∞, wouldn't be able to develop rated power at base speed, or even at high speed. The restriction on the dc supply such that the maximum applied voltage balances the back-emf at base speed is highly artificial. It is reasonable that the applied voltage at base speed be sufficient to overcome not only the back-emf but also the voltage drop across the internal impedance at base speed as is the case when the dc supply is determined using Eq. (5). When the dc supply is selected by Eq. (5), there will be sufficient voltage to develop rated power at base speed and a surplus power capability at high speed, that is $P_{\max}$ will exceed P_R. If desired, the surplus power capability can be made inaccessible by the control system.

For a finite CPSR requirement, the inequality in Eq. (18) at a relative speed, n, equal to the CPSR yields a minimum requirement on the motor inductance,

$$L_{\min} = \frac{\sqrt{V_{\max}^2 + CPSR\,(CPSR - 2)\,E_b^2}}{CPSR\,\Omega_b I_R} . \qquad (25)$$

And when $V_{\max}$ is determined from Eq. (8) and substituted into Eq. (18), the equivalent requirement is

$$L_{\min} = \sqrt{\frac{CPSR - 1}{CPSR + 1}} * \frac{E_b}{\Omega_b I_R} = \sqrt{\frac{CPSR - 1}{CPSR + 1}} * L_\infty . \qquad (26)$$

This expression shows that even for a modest finite CPSR, such as 4:1, the minimum inductance is $0.77 L_\infty$, which is a significant fraction of inductance for infinite CPSR.

In summary, the key parameter in determining the CPSR capability of the sinusoidal back-emf PMSM when driven by CPA is the motor inductance.

To illustrate the use of the various formulae, the design parameters of the motor design from Table 1 are applied to Eqs. (5), (8), (15), (19–22), (24), and (26) and presented below in Table 2.

10

Table 2. Calculations for the 6-kW FSCW SPM motor

Parameter		Value
P_R		6 kW
Ω_b		1413.7 elec rad/sec
E_b		49.45 Vrms
I_R		40.44 Arms
L		1300 μH
L_∞ Eq. (1)		865 μH
L_{min} (for CPSR=6.667) Eq. (26)		743.67 μH
n_{min} Eq. (19)		3.2588 (2933 rpm)
I_{min} Eq. (20)		22.4042 A
Characteristic Current $I_{CH} = E_b / X_b$ Eq. (22)		26.9070 A
V_{max} Eq. (8), Eq. (27)		89.23 Vrms/91.0 Vrms[*]
V_{dc} Eq. (5)		198.31 V/202.15 V
P_{max} Eq. (15), Eq. (24), Eq. (28)		7.21 kW / 7.03 kW[**]
CPSR (when driven by CPA)		∞

[*]The second value of V_{max} corrects for the winding resistance; i.e. V_{max} is computed as

$$V_{max} = \sqrt{(E_b + I_R R)^2 + (\Omega_b L I_R)^2} \ . \tag{27}$$

[**]With winding resistance included

$$P_{max} = \frac{3\left[V_{max} E_b - E_b^2 \cos\left(\tan^{-1}\left(\frac{X_b}{R} \right) \right) \right]}{\sqrt{R^2 + X_b^2}} \ . \tag{28}$$

When operating above base speed, the rms fundamental frequency voltage applied by the inverter is

$$V = V_{max} = \frac{\sqrt{2}V_{dc}}{\pi} \ . \tag{29}$$

The inverter lead angle depends on the dc supply voltage and the developed power and is found from Eq. (14) to be

$$\delta = \sin^{-1}\left(\frac{X_b P}{3V_{max} E_b}\right), \tag{30}$$

and from Eq. (12) the resulting rms motor current at speed, n, is

$$I = \frac{\sqrt{V_{max}^2 - 2nV_{max}E_b \cos \delta + n^2 E_b^2}}{nX_b}. \tag{31}$$

Note that at any finite speed, the rms current depends, at least to some degree, on dc supply voltage through its dependence on V_{max}, on the developed power through its dependence on δ, and on motor parameters, E_b and X_b; however, for high speed the rms current approaches the "characteristic current" given by

$$\lim_{n \to \infty} I = \frac{E_b}{X_b} = \frac{E_b}{\Omega_b L}. \tag{32}$$

2.6 LIMITATIONS OF CPA

The characteristic current depends only on motor parameters. When the inductance is sufficiently large, the characteristic current is less than the rated motor current, and this is what enables the CPA driven PMSM to operate with an infinite CPSR. There are, however, two potential drawbacks for wide CPSR drives controlled by CPA.

The first drawback is that at sufficiently high speed, the rms motor current approaches the characteristic current, which is independent of load, P. This means that the motor current is almost the same at no load as it is at full load. Consequently, the CPA drive cannot provide optimum "watts per amp" control at high speed and the efficiency may be poor when the load varies substantially at high speed.

One should expect that, if additional dc supply voltage were provided beyond the minimum necessary to produce rated torque at base speed, the result should be reduced motor current; however, as the speed increases the motor current approaches the characteristic current which is independent of the dc supply voltage. Thus, the second drawback is that increases in dc supply voltage beyond the minimum required to support base speed conditions are not effective in enhancing the efficiency of the wide CPSR drive at high speed.

If the motor inductance is the value given in Eq. (22) corresponding to an infinite CPSR, it follows from Eqs. (8), (10), (14), and (15) that

$$\begin{aligned}
V_{max} &= E_b\sqrt{2} \\
P_{max} &= P_R\sqrt{2} \\
\sin \delta &= \frac{P}{P_R\sqrt{2}} \\
\cos \delta &= \sqrt{1 - \sin^2 \delta}
\end{aligned} \tag{33}$$

Then the rms motor current under CPA control from Eq. (31) is given by

$$I = I_R \sqrt{\frac{n^2 - 2n\sqrt{2 - \left(\dfrac{P}{P_R}\right)^2} + 2}{n^2}} \quad . \tag{34}$$

Figure 3 shows how the reduction in current from Eq. (34) for reduced load is negligible at higher speeds.
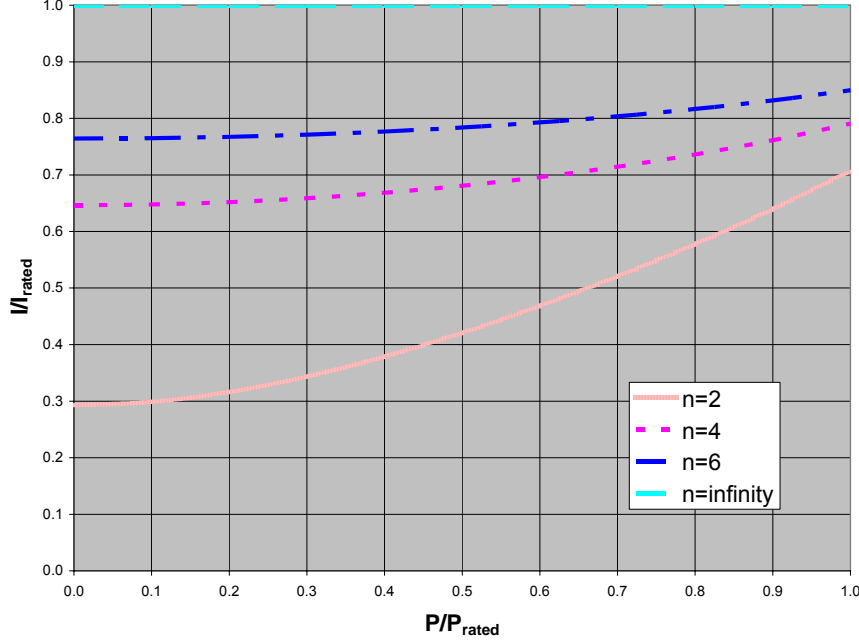
Fig. 3. Partial load operation of a PMSM under CPA control.

We would like a method that can make the rms current proportional to output power to reduce motor copper losses as well as the losses in the VSI inverter at partial load.

2.1 STEADY STATE CONTROL INCLUDING WINDING RESISTANCE AND ROTATIONAL LOSSES

The preceding analysis neglected winding resistance and rotational losses; consequently, it leads to compact expressions which provide considerable insight into the control of PMSM traction drives in constant torque and constant power modes. However, the control objective is to develop the required motor torque/power while minimizing the losses. We also wish to use a simple sine triangle PWM technique. In this type of PWM control there are two variables, the amplitude modulation index, m_a, and the inverter lead angle, δ. The value of m_a is defined as the ratio of the applied fundamental frequency control voltage to the peak value of a carrier switching voltage. The fundamental control voltage establishes the magnitude and frequency of the desired phase voltage. In this section, expressions, which include winding resistance and rotational losses, are given for m_a and δ for the PMSM traction drive. The availability of these expressions is useful for analyzing the performance of the new dynamic PWM controller.

13

During <u>low speed operation</u> at constant torque both the amplitude modulation index, which controls voltage magnitude and the inverter lead angle, can be adjusted. This allows the motor current to be placed in phase with the motor back-emf. Since all of the motor current produces torque, the rotor copper losses are minimized because the new control delivers maximum torque per amp. The required torque is

$$I_r = \frac{T}{3K_t} = \frac{T_{out} + T_{rot}(n)}{3K_t} \quad (35)$$

where T_{out} is the useful output torque and T_{rot} is the torque required to supply rotational losses. Using the equivalent circuit of Fig. 2 with $X = n X_b$, the applied fundamental frequency of the rms voltage required to drive this current into the motor is

$$V \angle \delta = nE_b + I_r \left(R + jnX_b \right)$$
$$= \sqrt{\left(nE_b + RI_r\right)^2 + \left(nX_bI_r\right)^2} \angle \tan^{-1}\left(\frac{nX_bI_r}{nE_b + RI_r} \right) \quad (36)$$

The necessary amplitude modulation index to provide this voltage is

$$m_a = \frac{V}{\dfrac{V_{dc}}{2\sqrt{2}}} = \frac{2\sqrt{2}\sqrt{\left(nE_b + RI_r\right)^2 + \left(nX_bI_r\right)^2}}{V_{dc}} \quad (37)$$

while the lead angle is given by

$$\delta = \tan^{-1}\left(\frac{nX_bI_r}{nE_b + RI_r} \right) \quad (38)$$

Note that the amplitude modulation index and the lead angle depend on speed and not on load.

Assuming full over-modulation, the constant torque control region ends at the "true base speed," n_{bt}, which causes the amplitude modulation index to be equal to $\dfrac{4}{\pi}$; consequently, the true base speed is implicitly defined using Eq. (37) as

$$\frac{4}{\pi} = \frac{2\sqrt{2}\sqrt{\left(n_{bt}E_b + RI_r\right)^2 + \left(n_{bt}X_bI_r\right)^2}}{V_{dc}} \quad (39)$$

which leads to a quadratic equation whose solution is

14

$$n_{bt} = \frac{\sqrt{\frac{2V_{dc}^2}{\pi^2}\left(E_b^2 + X_b^2 I_r^2\right) - R^2 X_b^2 I_r^4} - E_b R I_r}{\left(E_b^2 + X_b^2 I_r^2\right)} \tag{40}$$

.

<u>Above the true base speed</u> is the constant power mode. The torque producing component of current, which is in phase with the back-emf, required to sustain speed and load is given by

$$I_r = \frac{P}{3nE_b} = \frac{P_{out} + P_{rot}(n)}{3nE_b} \tag{41}$$

,

where P is the total required power, P_{out} is the useful shaft output power, and P_{rot} is the power supplied to rotational losses. Since the applied voltage is maximum in this mode,

$$m_a = \frac{4}{\pi} \tag{42}$$

while the appropriate inverter lead angle required to achieve power, P, is

$$\delta = \theta_z - \cos^{-1}\left(\frac{\frac{ZP}{3} + \left(nE_b\right)^2 \cos\theta_z}{nE_b V_{max}}\right), \tag{43}$$

where

$$V_{max} = \frac{\sqrt{2}V_{dc}}{\pi}$$

$$Z = \sqrt{R^2 + \left(nX_b\right)^2}$$

$$\theta_z = \tan^{-1}\left(\frac{nX_b}{R}\right) \tag{44}$$

.

The lead angle of Eq. (43) assures that the required power is developed but does not guarantee that the rms motor current magnitude is within rating unless the inductance is L_∞ or greater. Only having motor phase inductance greater than L_∞ will guarantee current lower than rated motor current [4].

Equation (43) is derived from

$$I = \frac{V\angle\delta - E\angle 0}{R + jnX_b} = \frac{V\angle\delta - E\angle 0}{Z\angle\theta_z} = \frac{V\angle(\delta - \theta_z) - nE_b\angle(-\theta_z)}{Z}, \tag{45}$$

and the equation for total per-phase power that the motor must provide,

$$\frac{P}{3} = Re(\widetilde{EI}^{*}) = Re\left(\frac{nE_bV\angle(\theta_z-\delta)}{Z} - \frac{(nE_b)^2\angle\theta_z}{Z}\right) = \frac{nE_bV\,cos(\theta_z-\delta)}{Z} - \frac{(nE_b)^2\,cos\,\theta_z}{Z}, \quad (46)$$

which, with $V = V_{max}$, leads directly to Eq. (43).

Figure 4 shows the algorithm for simulating a vehicle's performance when it is controlled by ORNL's simple model-based control scheme. It assumes that the motor parameters, which include inductance, resistance, and back-emf constant, as well as the quadratic expression for losses are known. When this control is used for laboratory testing the PWM/Inverter block is replaced gate drives and inverter switches, the Motor Model block is replaced by the motor itself, and the Vehicle Dynamics block is replaced by the dynamometer with its torque absorption capability and position and speed sensors. The only remaining change when this control is used in a hybrid electric vehicle (HEV) on the road is that the Vehicle Dynamics block is replaced by the vehicle itself.
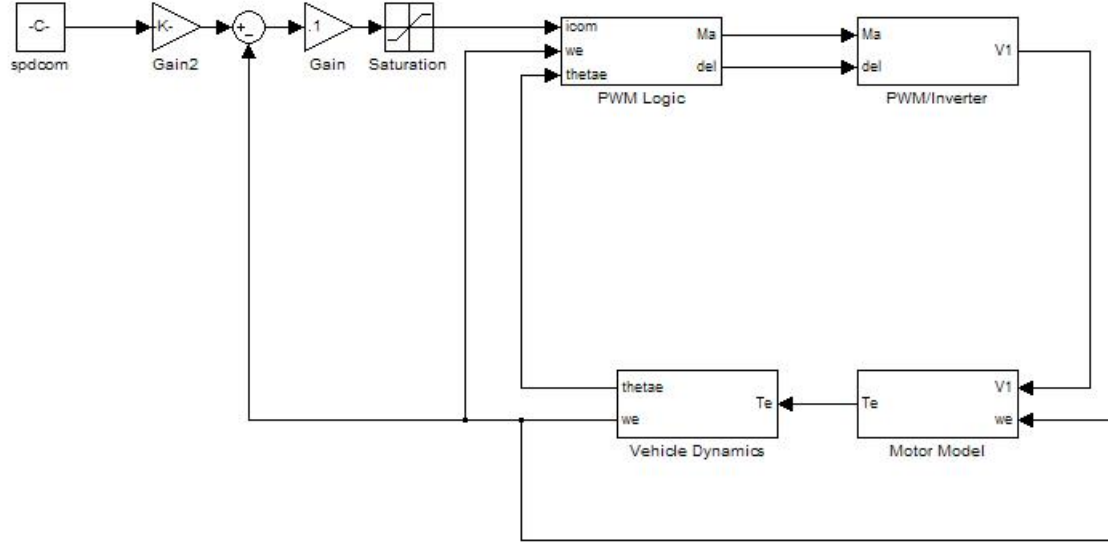
Fig. 4. Simulation of vehicle performance using ORNL's sensorless control.

Control of the vehicle's performance in the simulator is straightforward. The operator supplies a request for a change in speed with the speed command, spdcom, to which a gain is applied so that the mechanical speed matches the electrical speed, ω_e. The electrical speed is compared with the actual speed of the vehicle to determine the speed correction. A gain of 0.1 is applied to the speed correction to provide a linear command current, icom, which is not allowed to exceed the rated current.

Below true base speed whose expression is presented in Eq. (40), the modulation coefficient, Ma, is given by Eq. (37) and the angle, del, by which the PWM voltage leads the back-emf is given by Eq. (38) in terms of speed and current, or by Eq. (43) with V_{max} replaced by V in terms of speed and power. Equation (36) is the expression for the PWM voltage, V1.

Above true base speed the modulation index is $4/\pi$ from Eq. (42) and the inverter lead angle, del, required to achieve power, P, is given by Eq. (43). The PWM voltage, V1, has its maximum value, $V_{max} = \sqrt{2}V_{dc}/\pi$, from full over-modulation.

The PWM voltage and the rotational frequency determine the torque, Te, in Fig. 4. In the Motor Model block, the user may alternately specify the power, which is related to the torque by the equation, $P = T \omega_e$. In the simulation, the Vehicle Dynamics block applies the torque determined by Eq. (35) to calculate the new value of ω_e and keeps up with the reference back-emf angle to which the PWM voltage lead is applied.

3.0 EXPERIMENTAL SETUP

The tests performed to demonstrate ORNL's parameter based control scheme, which do not use current sensors or phase voltage sensors, employed a new inverter and an upgraded OPAL-RT system. Both systems performed reasonably well, although the inverter was used at a fraction (6 kW) of its power capability (150 kW) and the OPAL-RT system encountered problems generating a stable PWM voltage waveform as the control system approached a modulation index of 1.

The new inverter was a VLT 5252 purchased from Danfoss. Two sets of interface cards compatible with the Danfoss VLT 5252 inverter were ordered from Aalborg University in Denmark. One of these cards converts digital gate signals from the OPAL-RT controller to fiber optic signals and the second card converts the fiber optic signals back to digital signals. This card also monitors over voltage, over current, over temperature, and if required shuts down the inverter.   Purchase of these boards and inverter was guided by the University of Wisconsin at Madison (UWM) who has had very good experience with them. A set of dc connectors was added inside the inverter housing to allow power from a 600 V, 600 A Robicon dc power supply to be connected directly to the inverter's dc link. Although not used during this testing, the inverter dc link can be supplied by rectified, 3-phase, 480 V power from a variac.

Prior experience with OPAL-RT's inability to generate a stable voltage waveform forced us to consider use of an external signal generator with a sine reference wave and a triangular carrier wave and a comparator. Although this approach works for motors with low numbers of poles, it adds delay time which becomes unacceptable as the number of poles increases for FSCW motors; consequently we upgraded our OPAL-RT system. The best chance for generation of stable PWM waveforms by the OPAL-RT computer, which was supported by OPAL-RT, involves trade-up of our existing computer, which has a 400 MHz bus speed, with replacement by a 3.2 GHz target PC, which has an 800 MHz bus speed and a QNX 6.2 operating system. The old I/O cards with preprogrammed PWM generation were replaced by OPAL-RT's field programmable gated array (FPGA)-based I/O cards to generate balanced PWM.

Figure 5 is a block diagram of the electrical connections. The fused disconnects and wire sizes were carefully considered during wireup of the inverter. Figure 6 is a block diagram of the test cell and control room. Note that current and voltage sensors were only used for power measurement and not for control purposes. Access to the room during operation of the motor was not allowed except at speeds below 50 rpm. A GP-IB cable transmitted data from the Yokogawa PZ400 power analyzer to a data readout program in the control room. The DynSystem panel in the control room was used to control either speed or torque load. Initially the dynamometer was used to drive the motor for determination of the voltage constant and no-load power losses. Also the phase resistance, phase inductance, and magnetic intensity of each magnet were measured. Figure 7 shows the motor, dynamometer, and test hardware.

Figure 8 is the user interface model. It displays speed of the motor, direction of the motor rotation, frequency, and the three control variables generated by the controller which are modulation index, voltage lead angle, and commend current. Using this interface, all of the following commands may be changed; the speed command; the offset angle used with the incremental encoder; the Enable command, which enables inverter switching; and the Break command, which shuts down the motor in case of emergency.

3 Φ AC, utility supply 480 V, 200 A (Dyne rooms L102 and L103)

20 A Circuit breaker

SC* : 4 Current and
4 Voltage Sensors

#12 AWG

Available:
1 AWG from test bedplate to building ground

20 A Control logic power supply

#4/0 AWG
Good for
dc 230 A
(~1/3*600 A)
●Lug 88 is negative
●Lug 89 is positive

Test bedplate

Motor (6 kW) rated current, @ 60 A, on test bedplate

#1 AWG
Good for 100 A

SC*

G

89   88

U   V   W

Robicon drop 600 V, 200 A fused disconnected

Fused breaker
600 V , 200 A disconnect

100 A fuse with reducing clips from 200 A to 100 A.

4/0 AWG
Good for 200 A

Available: Two #1/0 AWG from Robicon frame to building ground.

Fig. 5. Overall motor/inverter connection schematic.

19
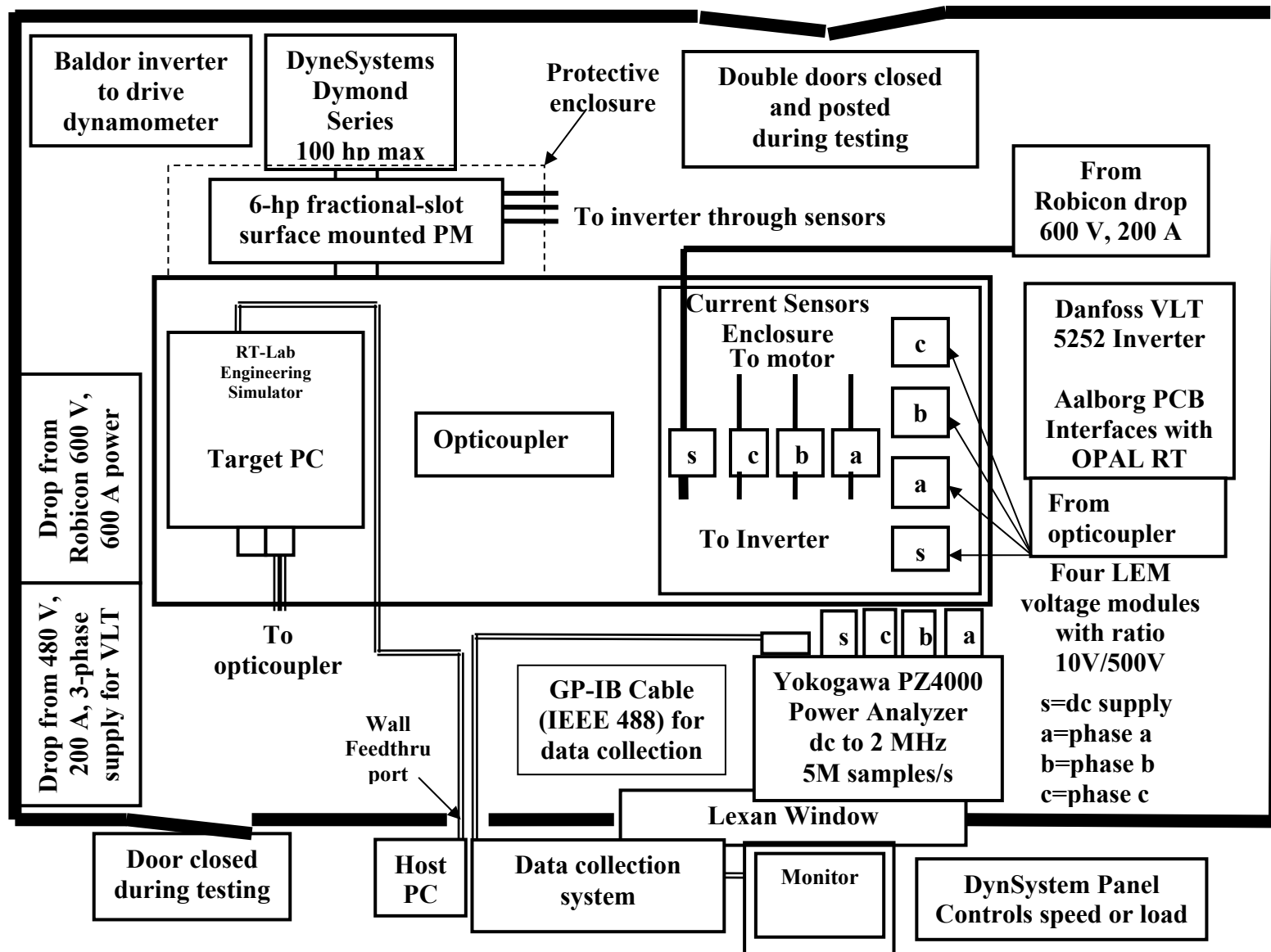
Fig. 6. Overall drive schematic of motor, inverter, sensors, power analyzer, and OPAL-RT control system.
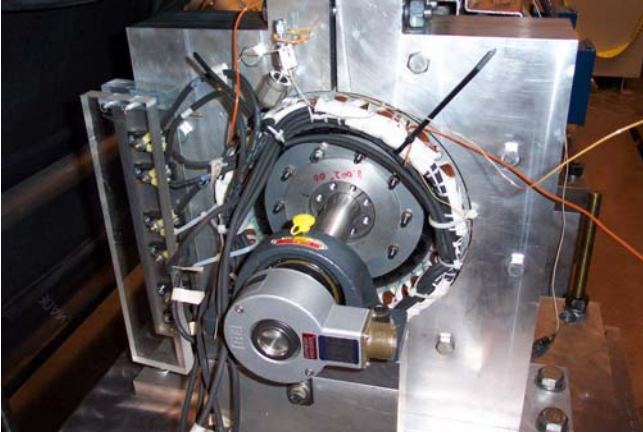
(a) A 6-kW fractional-slot SPM with concentrated windings.

(b) FSCW SPM motor connected to dynamometer.
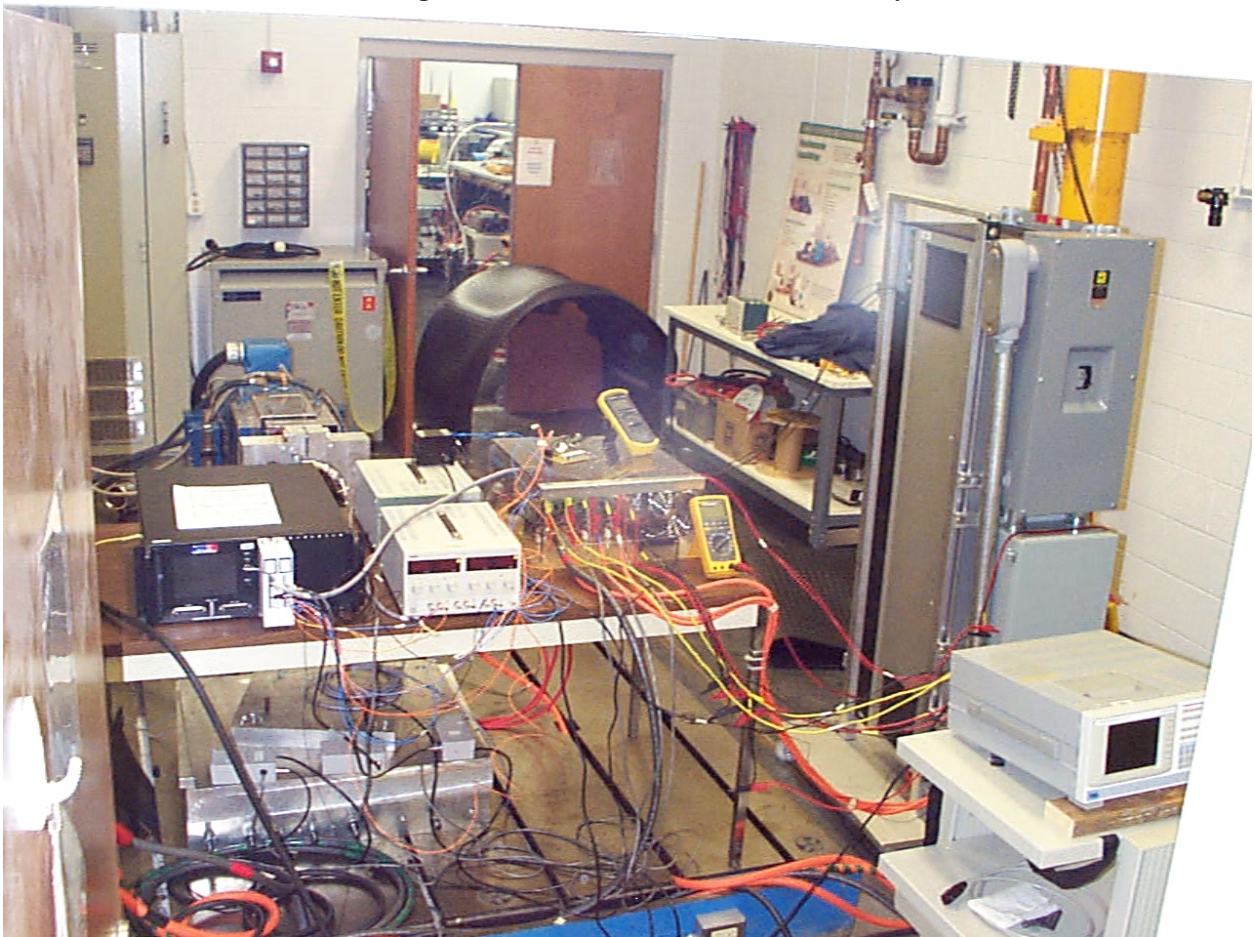
(c) OPAL-RT target control PC, current sources, sensor box, inverter, and power analyzer.

Fig. 7. Overall test setup.
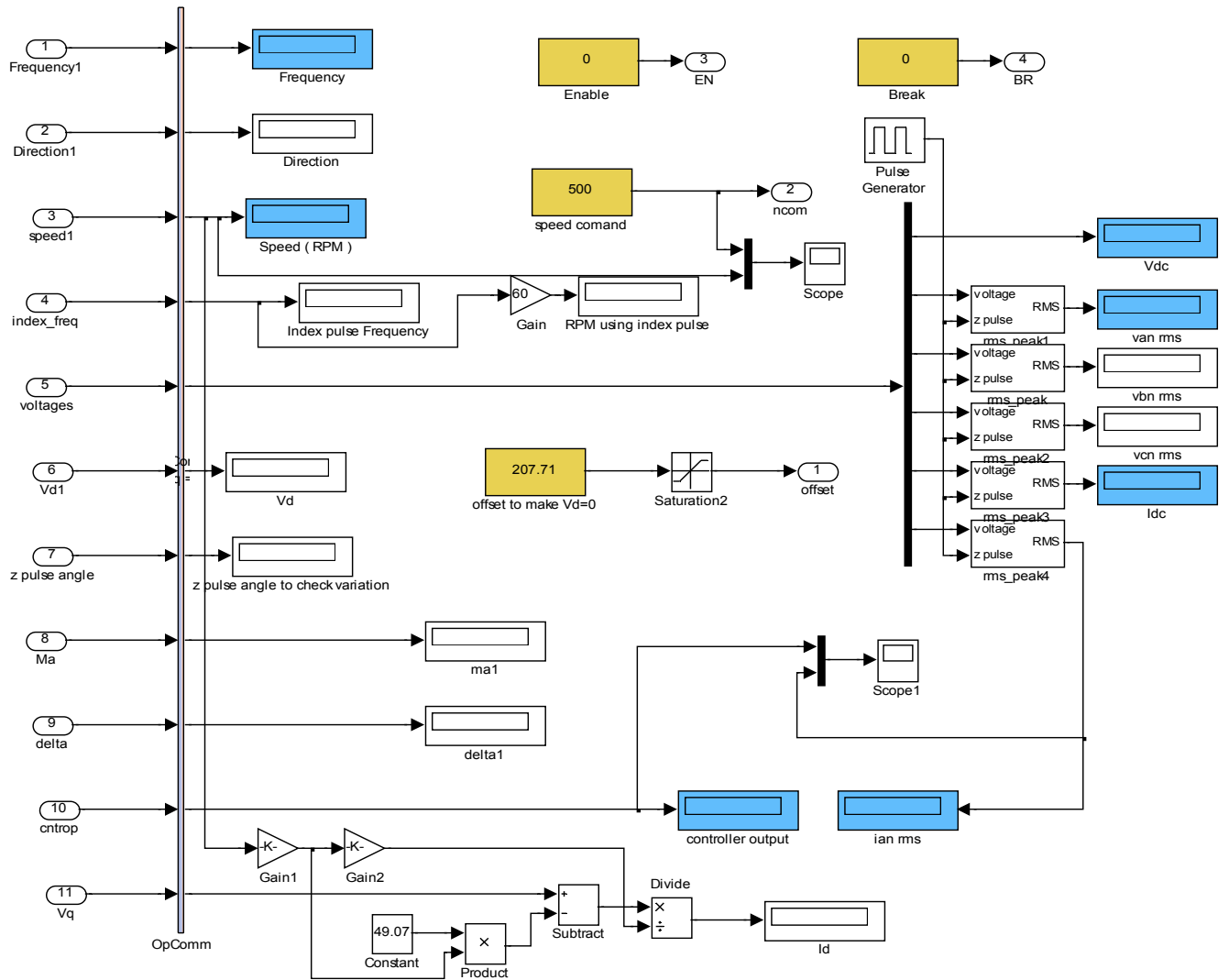
Fig. 8. User Interface Model.

Figure 9 is the data acquisition and controller models. The top third of the model is an encoder interface, which acquires A, B, and Z pulses and calculates speed, rotor angle, direction of the rotation, and frequency. An incremental encoder was used to feed the speed and the rotor position back to the controller. Incremental encoders have three output pulses; A, B, and Z. This particular encoder has 1024 A and 1024 B pulses per mechanical revolution. Since there is a 90° offset between pulses A and B, if the logic circuitry allows the counter to count each rise and fall of both A and B, the number of pulses per revolution will be 4096, which allows a fourfold increase in resolution for the speed measurement. There is also one reference pulse, which is called a Z or zero pulse, for each mechanical revolution. This Z pulse is usually used to reset the rotor angle measurement counter. Measurements were carried out to find an offset angle between the reference Z pulse of the incremental encoder and the zero crossing of the back-emf waveform. Initially, the motor was driven by the dynamometer so that the back-emf and Z pulse could be displayed on the oscilloscope. Discussions with UWM revealed that this offset angle is not constant and it varies with the speed. Another more accurate way to calculate this offset angle is to

display the motor, the back-emf waveform, and the sine waveform generated by the controller on the oscilloscope while adjusting the offset angle in the controller until both waveforms overlap. Since this new OPAL-RT system does not have an analog output card, this angle was adjusted manually as needed to obtain the desired overlap.
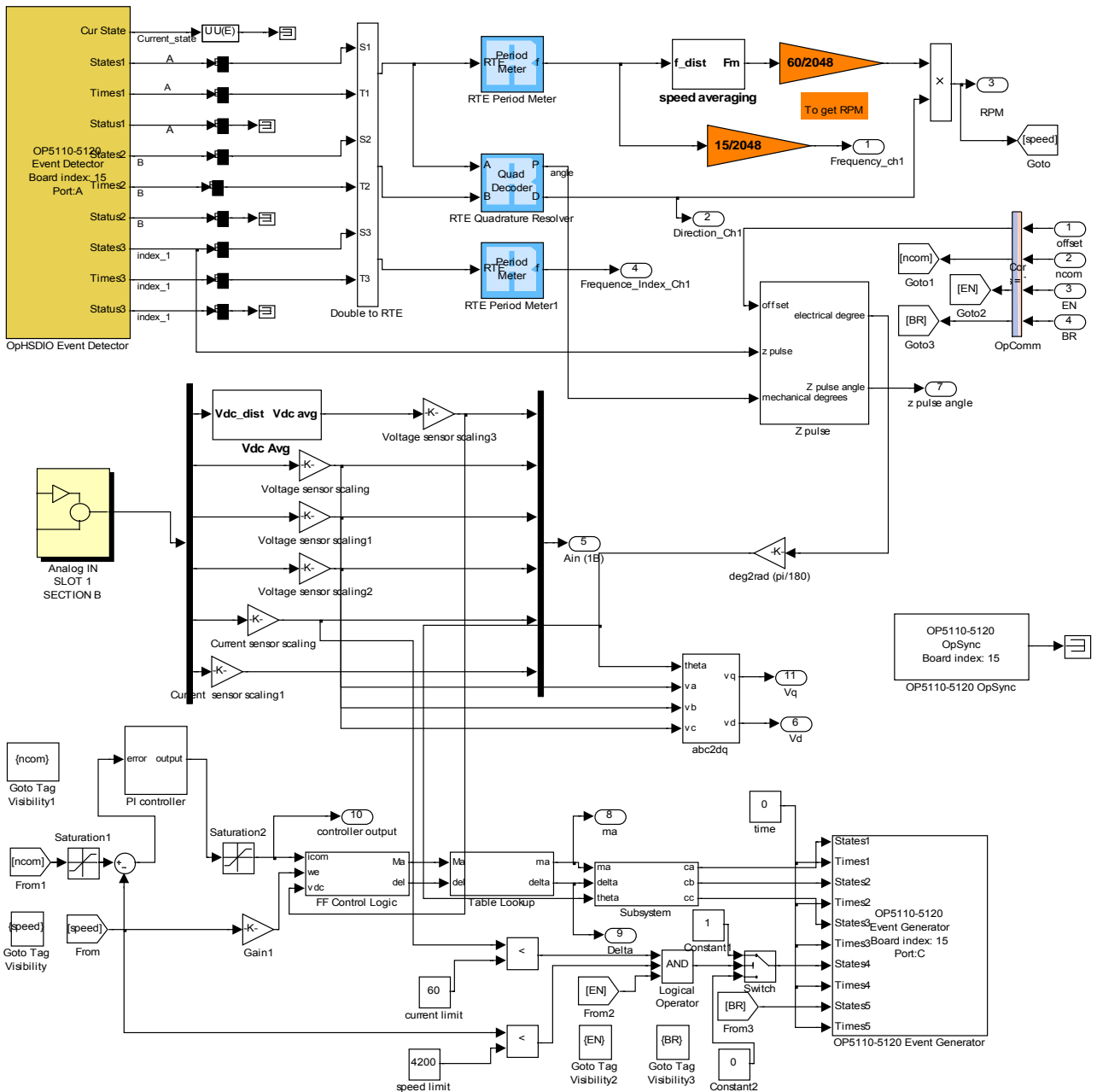
Fig. 9. Data acquisition and controller models.

The middle third of Fig. 9 acquires the dc supply voltage, dc supply current, phase voltages, and current. The lower third of the model is the controller, which accepts the speed command, compares it with speed feedback and by using the reference rotor angle generates the modulation index and voltage lead angle for PWM switching. Using this modulation index and the voltage lead angle, gate signals are generated, which produce the desired PWM switching.

23

Figure 10 is a more detailed diagram of the FF Control Logic block in Fig. 9.
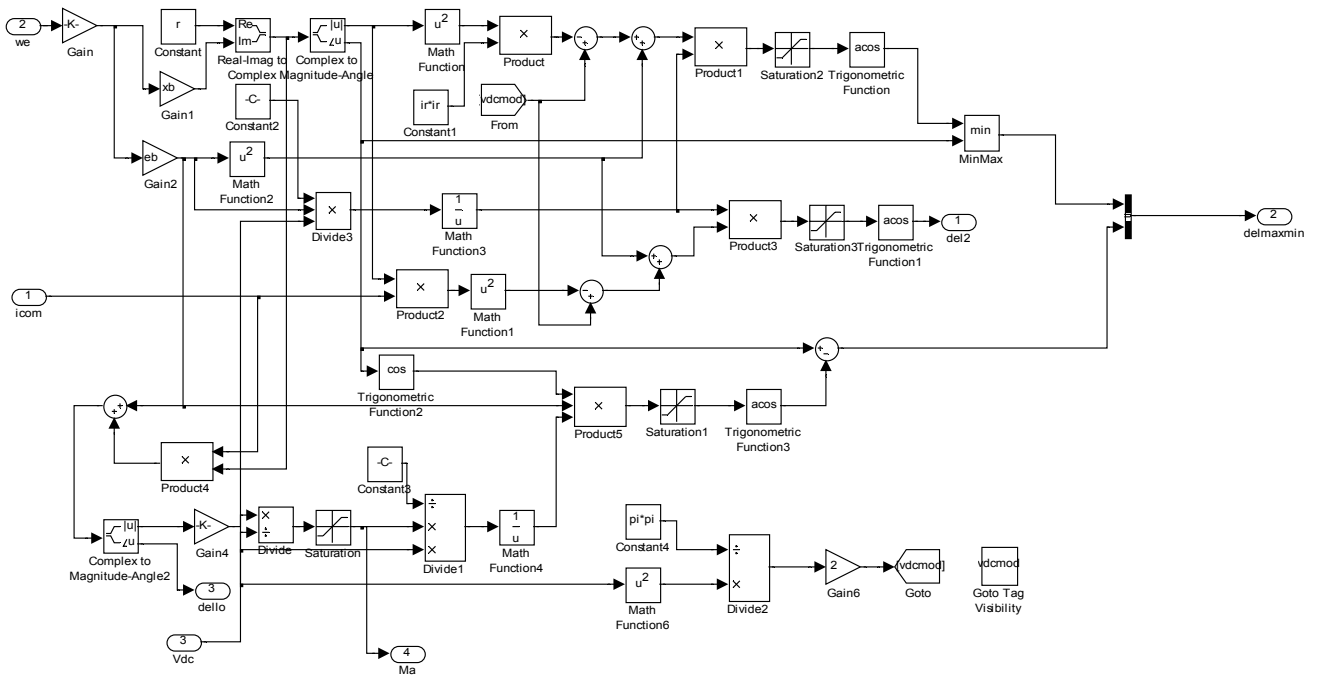
Fig. 10. Detailed controller model.

Figure 11 is a detailed diagram of the sine triangle PWM generator.
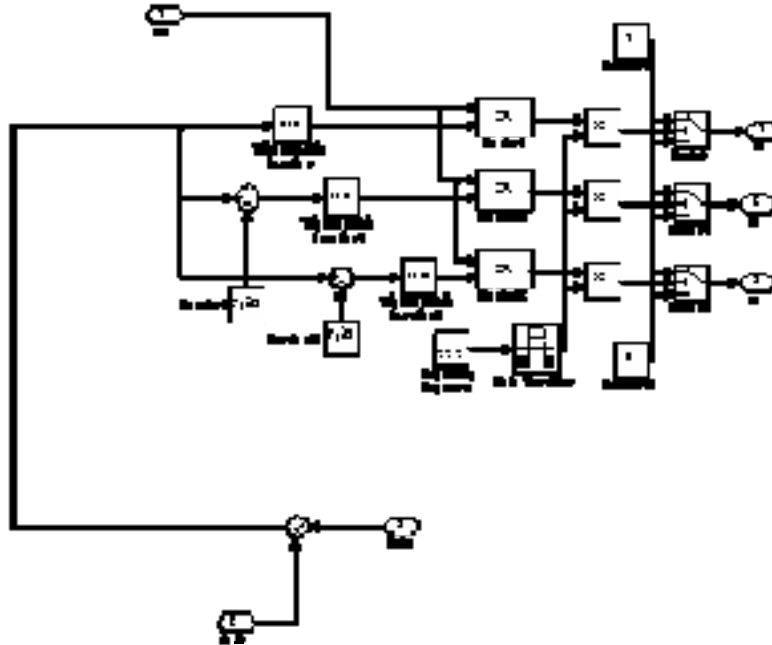
Fig. 11. Sine triangular PWM generator.

A typical startup procedure was:

1. Connect the 3-phase, 480 V auxiliary power source to provide power to the inverter's internal circuitry followed by a restart using a push button on the Alborg card, which is mounted in the inverter.
2. Turn motor and dyne cooling system ON.
3. Turn the dyne power supply ON.
4. Compile the Simulink based control model in the command station and download it to the target PC.
5. Start the controller without enabling inverter gate switching.
6. Connect dc power supply and ramp it up to the desired dc link value to avoid high inrush currents.
7. Start dyne in speed mode and ramp up the motor speed to 400 rpm.
8. Release the dyne by turning the speed mode OFF and ENABLE the inverter gate signal switching. After this, the controller should adjust the motor speed to the command value. Since an incremental type encoder was used, this was done to avoid initial rotor position detection problems.
9. Turn the dyne back ON but in torque mode.
10. Start loading the motor to desired load conditions.

The Yokogawa PZ4000 power analyzer was used to measure dc power, motor input power, and motor output power.

4.0 EXPERIMENTAL RESULTS

1. Figure 7 shows overall drive setup.

2. From Table 3 it can be seen that the measured phase winding resistance and inductance are close to the analytical values and experimental values published by UWM.

3. Figure 12 shows measured no-load losses also in Table 3. At higher speeds, these losses are about 15% of the rated motor power.
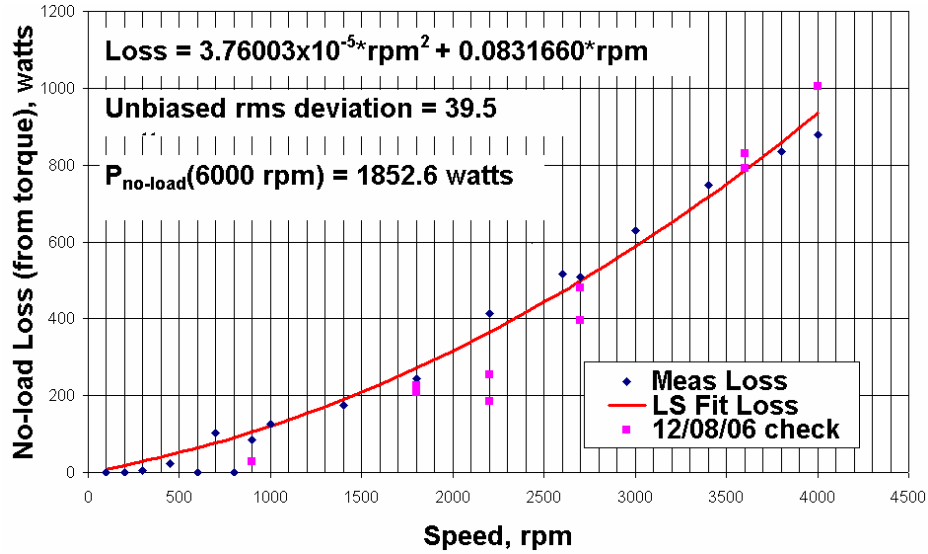
Fig. 12. No-load losses of 6-kW fractional-slot SPM motor with concentrated windings.

4. Figure 13 shows measured phase back-emf (V_{rms}) versus speed and a least-squares fit. The voltage constant, k_v, is about 0.0547.
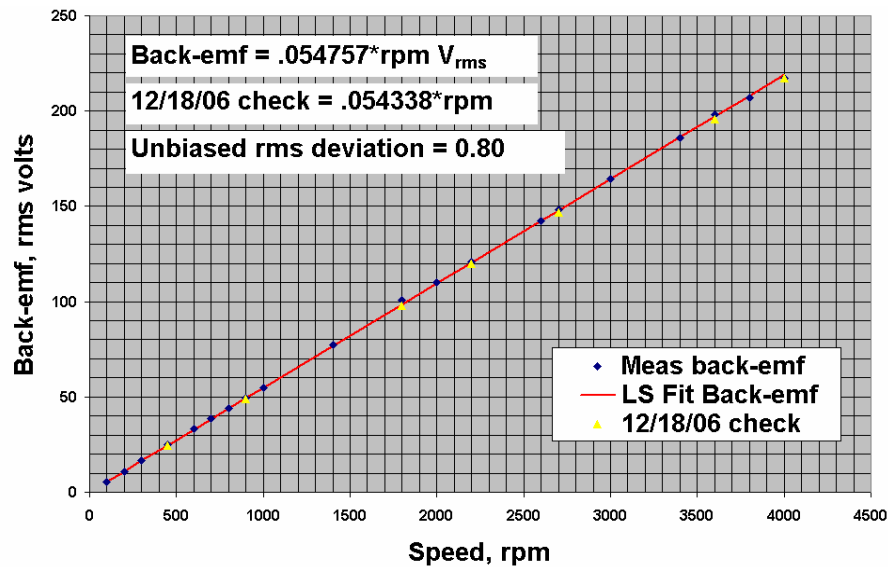
Fig. 13. Back-emf of 6-kW fractional-slot SPM motor with concentrated windings.

26

Table 3. Measurements of motor parameters, back-emf constant, and no-load losses

Speed	Power measured	Power calculated	Torque	Peak - Peak Amplitude	Cycle RMS	Fundamental compone	V3	Frequency
(RPM)	(Watts)	(Watts)	(Nm)	(Volts)	(Volts)	Volts (RMS)	3rd Hrmnc	(Hz)
							@ 12.73%	
100	0	0	0.0	13.00	5.53			25
200	0	0	0.0	27.00	11.00			50
300	0	6.2832	0.2	40.00	16.54			75
450	0	23.5619	0.5	64.00	24.91	24.47	3.15	112.9
600	0	0	0.0	81.00	33.05			150
700	100	102.6254	1.4	95.20	38.60			175
800	0	0	0.0	108.00	44.02			200
900 (Base Speed)	100	84.823	0.9	125.60	49.64	49.45	6.3	224.7
1000	100	125.6637	1.2	135.00	55.00			250
1400	200	175.9292	1.2	190.40	77.10			350
1800	200	245.0442	1.3	254.00	100.80	98.75	12.75	449.2
2000	100	146.6077	0.7	268.80	110.10			500
2200	400	414.6904	1.8	296.40	121.00			550
2600	500	517.3156	1.9	348.80	142.60			650
2700	500	508.938	1.8	375.00	148.20	149.1	18.75	674.8
3000	600	628.3185	2.0	399.60	164.20			750
3400	700	747.6991	2.1	456.00	185.90			850
3600	800	791.6813	2.1	498.00	197.90	197.4	25.125	899.5
3800	800	835.6636	2.1	508.80	206.90			950
4000	900	879.6459	2.1	532.80	217.30			1000
	Resistance			Inductance,Frequency ≈ 1kHz				
				Voltage = 1V	Voltage = 10 V			
Phase A	0.07535 Ω	75 mΩ		1.13 mH	1.185 mH			
Phase B	0.07683 Ω	76 mΩ		1.18 mH	1.1899 mH			
Phase C	0.07560 Ω	75 mΩ		1.14 mH	1.1968 mH			
Analytical prediction		63 mΩ		1.03 mH				
FEA prediction				1.16 mH				
Wisconsin measured		71 mΩ		1.3 mH				

5. Since back-emf measurements were carried out with neutrals unconnected, a small contribution from the 3rd harmonic recorded in Table 3 manifests itself in Fig. 14 by flattening the top of the waveform. It also appears directly in the fast fourier transform (FFT) analysis of Fig. 15.
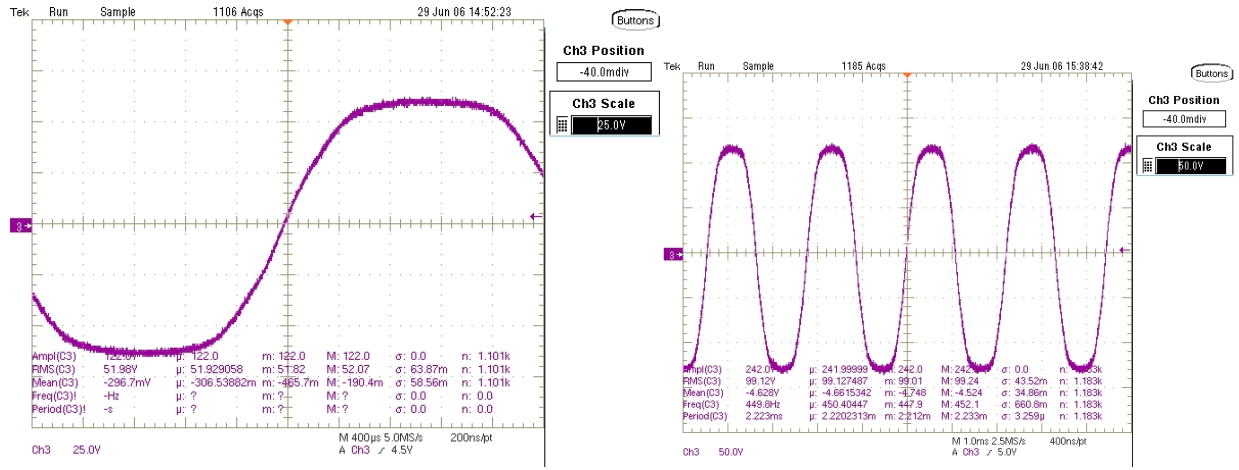
| (a) 900 rpm. | (b) 1800 rpm. |

Fig. 14. Back-emf waveforms.
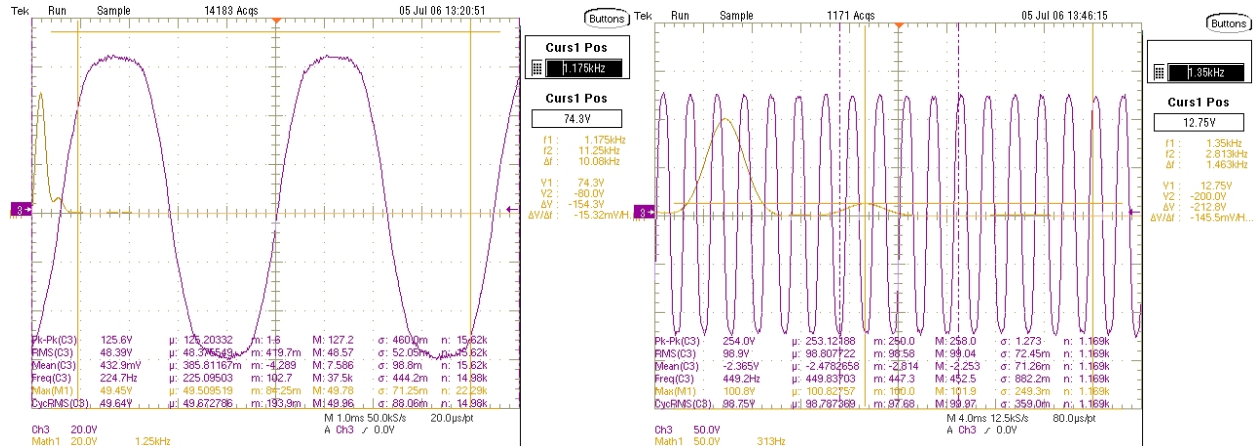
| (a) 900 rpm. | (b) 1800 rpm. |

Fig. 15. Back-emf waveforms with their FFT spectral content.

6. Figure 16 shows the symmetry of phases a, b, and c.

28

(a) Phases a and b.   (b) Phases b and c.
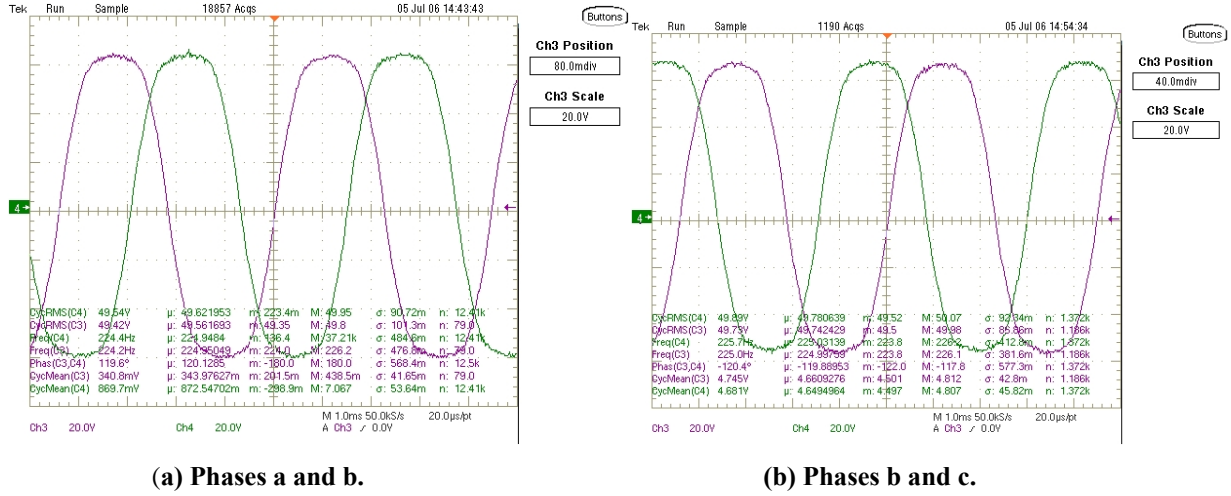
Fig. 16. Phase voltage waveforms.

7. Above base speed, Fig. 17 shows that total current monotonically decreases asymptotically approaching the "characteristic current" given by Eq. (21). Total no-load losses, which have no copper losses, do include a contribution generated by the magnets from eddy current and hysteresis losses in the core and magnets. Above base speed losses are less than the corresponding no-load losses because, under "vector control terminology," the contribution to copper losses from torque producing current, I_q, is compensated by reduced core losses which result when the magnetic flux that generates core losses is reduced (weakened) by increased dc, I_d. Separation between the no-load loss curve and total loss measurements when under load widens with speed because at constant power, I_q decreases with speed further reducing copper losses and I_d increases with load further decreasing core losses. Another effect that reduces both copper and core losses as speed increases is skin effect. This is the tendency which becomes more pronounced as speed increases for current to flow closer to the surface not only in the copper conductors but also in the core material and magnets.

29

@ 300 V
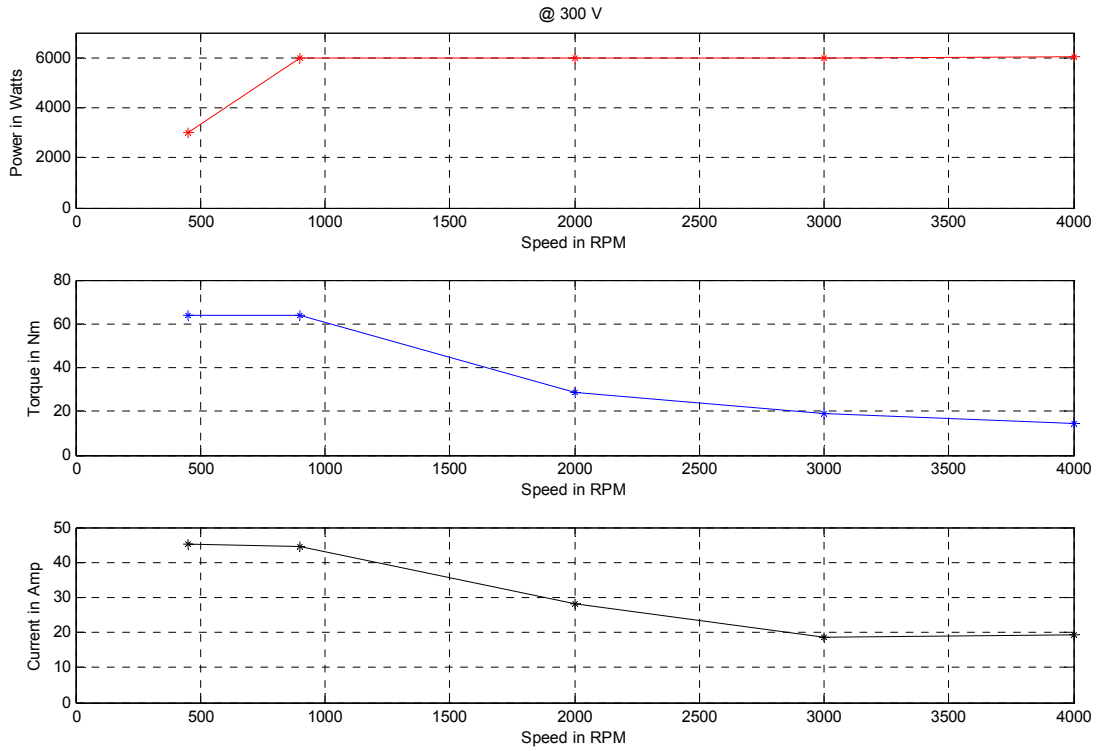
Fig. 17. Measured motor characteristics.

8. Figure 18 shows the motor response to the speed change command. Since the control has no regenerative mode, no controller action governed deceleration resulting in slower response than occurred during acceleration.
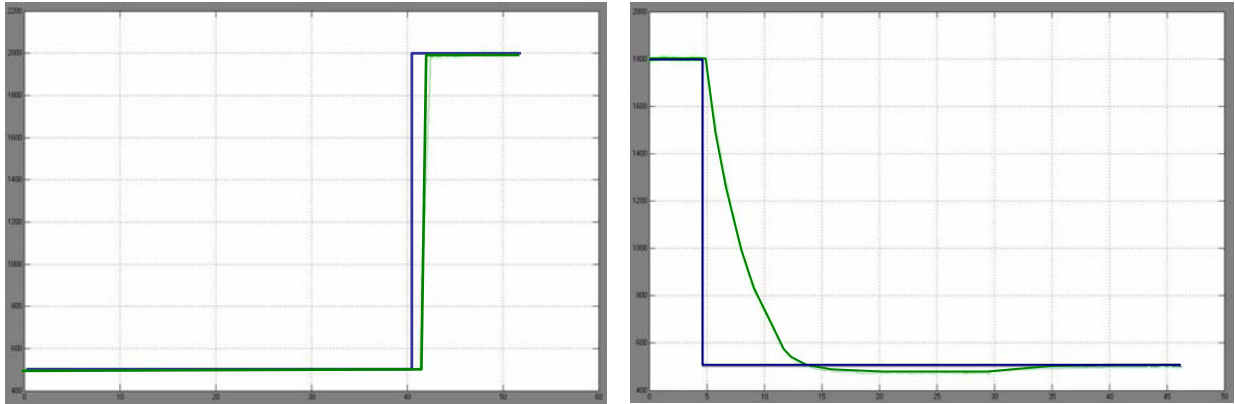
Fig. 18. Speed tracking with purple line for speed command and green line for motor response.

9. Figure 19 shows measured losses for different load conditions. Since the applied dc voltage was greater than $V_{dc-min} = 202.15$ volts from Eq. (5), true base speed given by Eqs. (6) and (40) exceeds the actual base speed, which is 900 rpm. True base speed is about 1113 rpm for a supply voltage of 250 V_{dc}, and about 1335 rpm for 300 V_{dc}. True base speed is the speed above which the motor will operate in field weakening mode [5]. It can be seen from Fig. 19 that losses below base speed exceed

30

no-load losses and also they increase as the load increases. This is caused by copper losses, which increase with the square of the current.
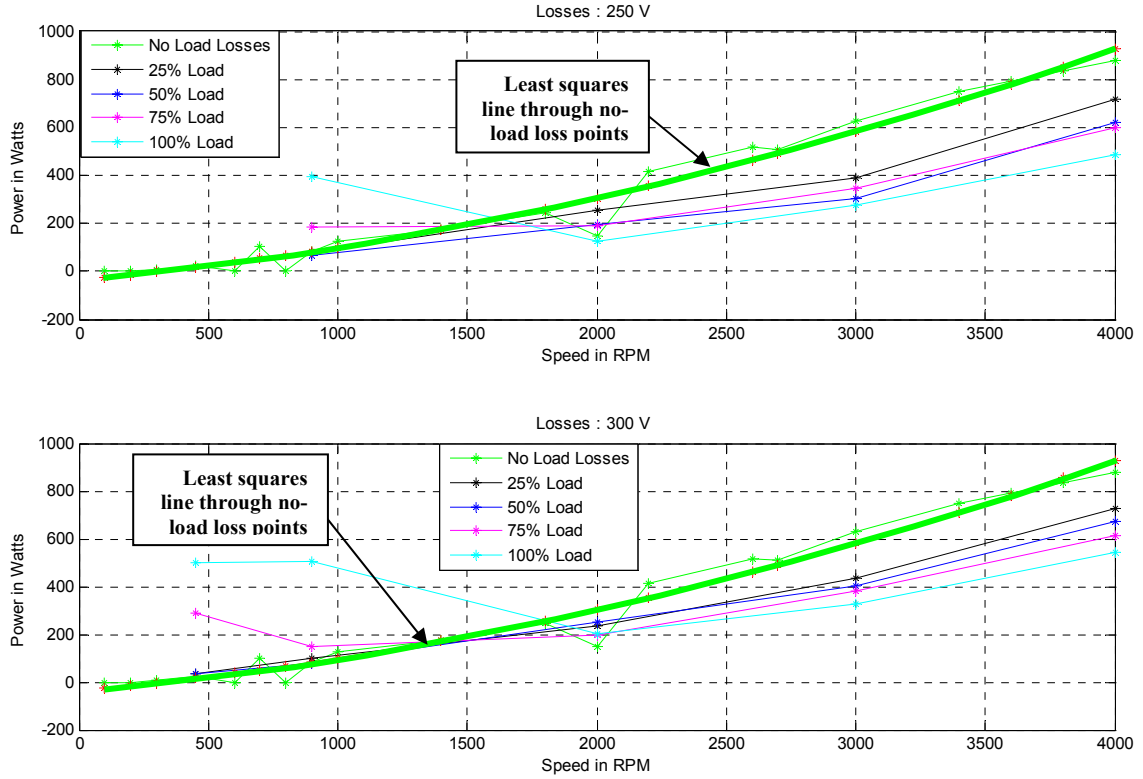
Fig. 19. Measured motor losses.

10. Figure 20 shows motor efficiency with supply voltages of 250 V_{dc} and 300 V_{dc}. The solid color surface (filled) corresponds to the 250 V_{dc} supply and the white surface (unfilled) corresponds to 300 V_{dc} supply. Efficiencies are about 2% better with 250 V_{dc} than with 300 V_{dc}. Efficiency drops to 70% at 4000 rpm at 25% load. This is a limitation because, as explained earlier, at higher speeds current approaches the characteristic current, which is independent of the load conditions and depends only on the motor parameters, inductance, and base speed back-emf. So at speeds above true base speed, copper losses are roughly constant while iron core losses increase with speed under CPA with little or no relief at partial loads. UWM has developed a method to improve motor efficiency at partial loads, especially at higher speeds [6] by applying vector control to increase the component of dc, which weakens the magnetic field that generates core losses.

31
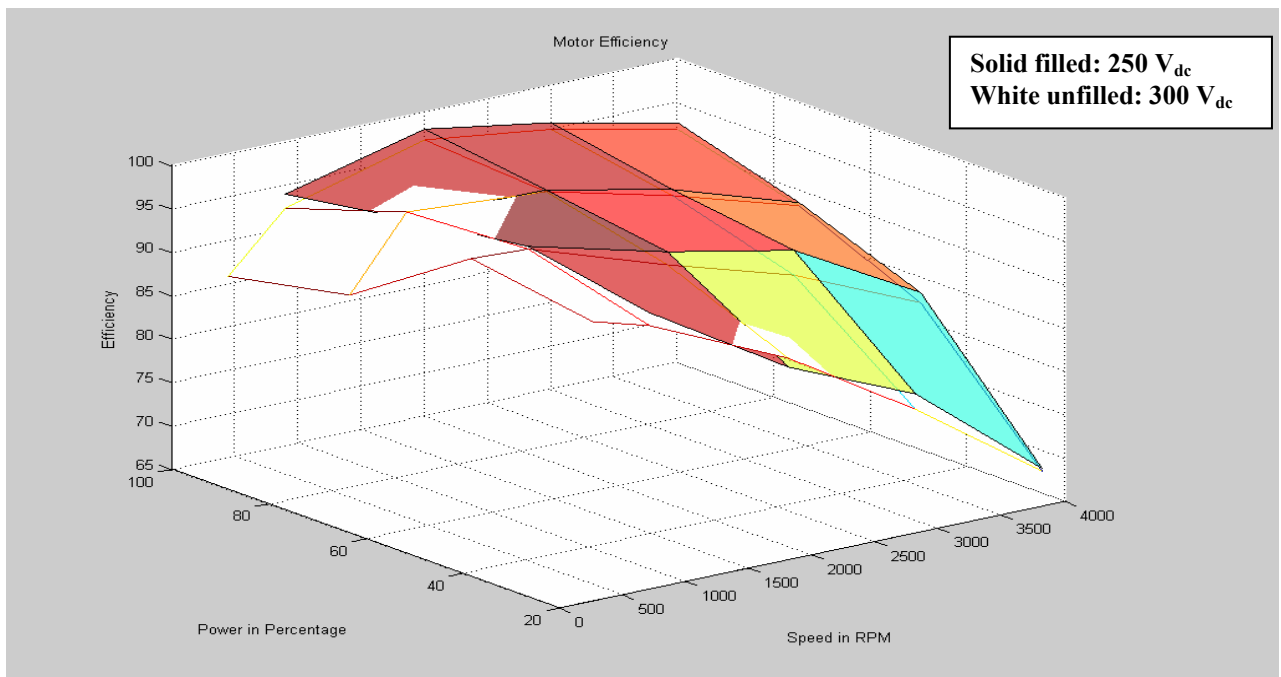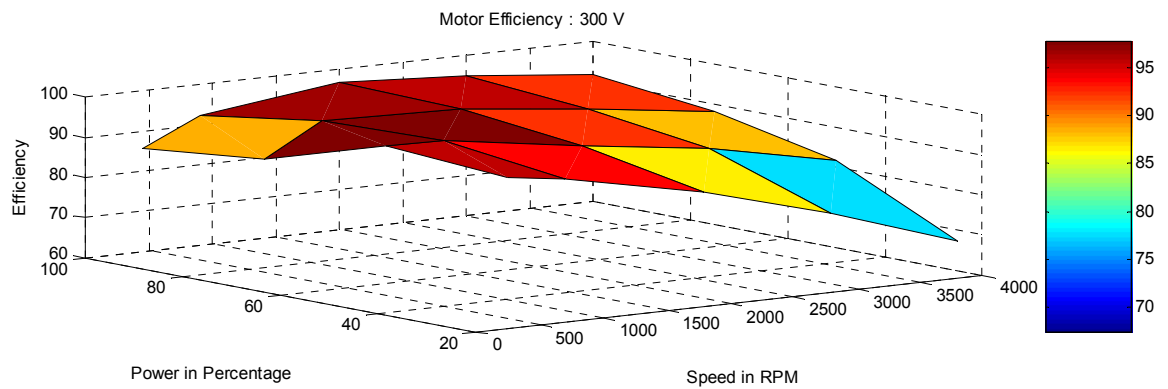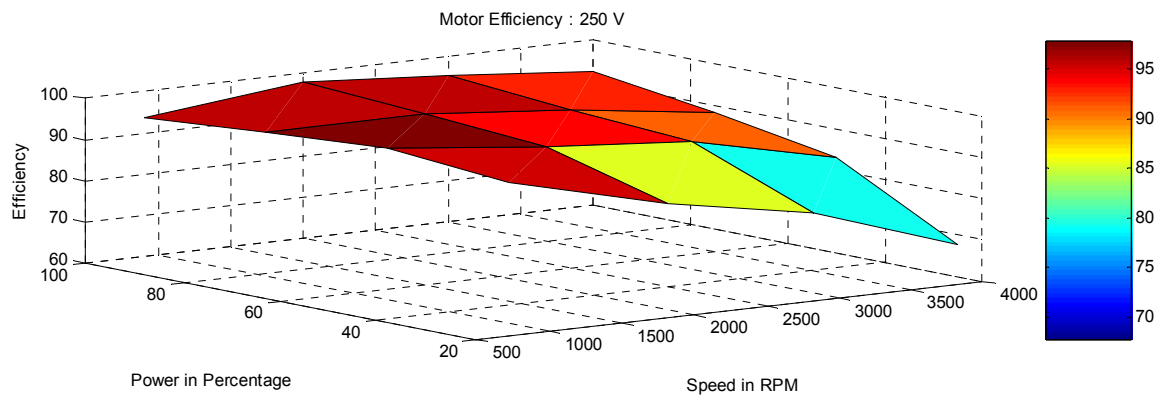
Fig. 20. Motor efficiency comparison at supply voltages of 250 V$_{dc}$ and 300 V$_{dc}$.

11. Figure 21 shows inverter efficiencies with supply voltages of 250 V_{dc} and 300 V_{dc}. Above true base speed, PWM goes into a six step operation for which the modulation index, m_a, becomes $m_a = 4/\pi$. At the reduced carrier frequency intrinsic to a six-step operation, switching losses are minimum and since the 20 A current is also low, conduction losses are very low. It can be seen from Fig. 21 that, above true base speed, inverter efficiency is about 99%.
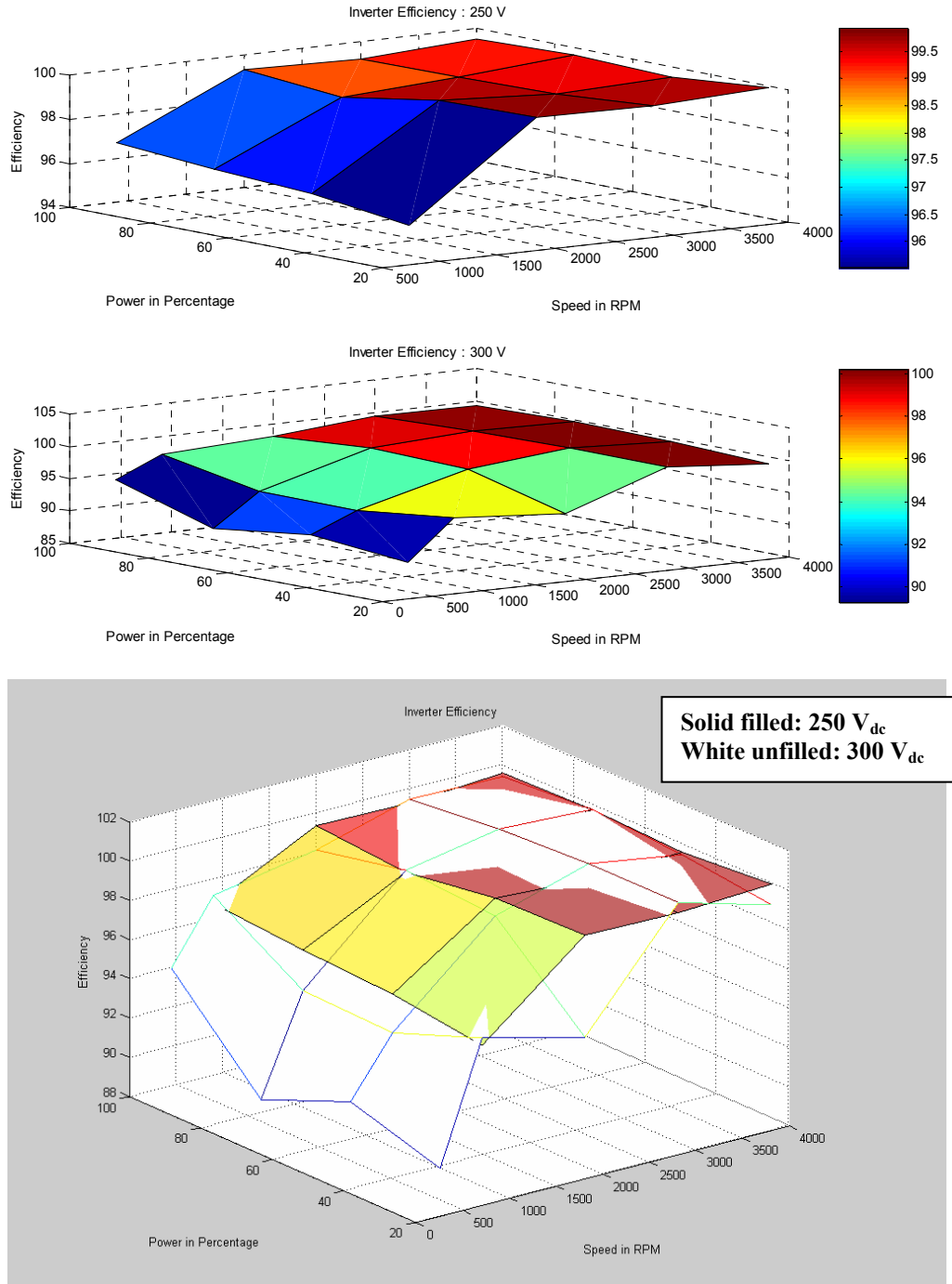
Fig. 21. Inverter efficiency comparison at supply voltages of 250 V_{dc} and 300 V_{dc}.

12. Figure 22 shows overall drive efficiency, which is slightly better at a supply voltage of 250 than at 300 V_{dc}.
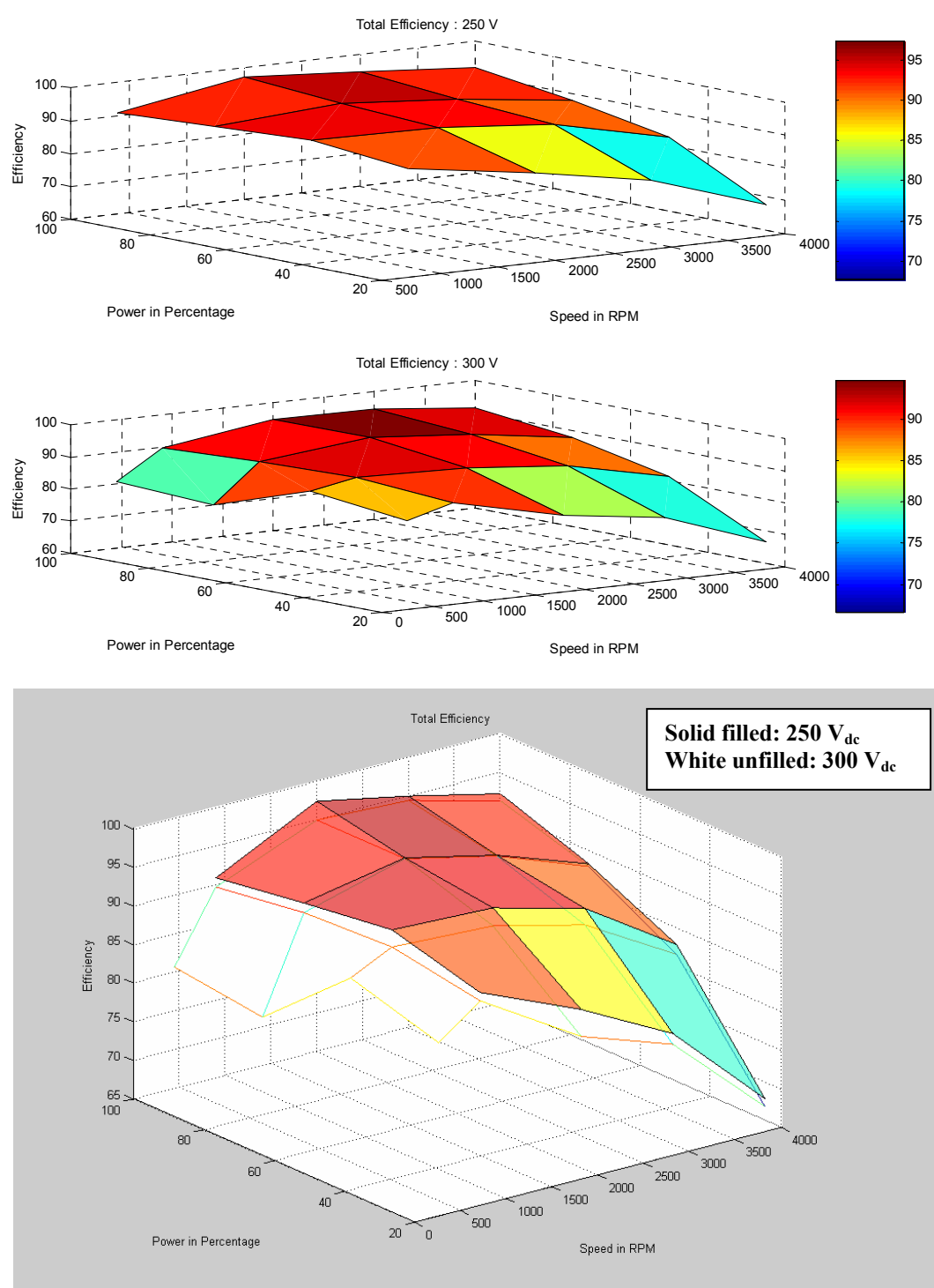
Fig. 22. Drive efficiency comparison at supply voltages of 250 V_{dc} and 300 V_{dc}.

34

Tables 4, 5, 6, and 7 summarize the data plotted in Figs. 15, 16, and 17. The supply voltage for the data in Tables 4 and 5 was 300 V$_{dc}$ and the supply voltage for the data in Tables 6 and 7 was 250 V$_{dc}$. Tables 4 and 6 include data for 25% and 50% loads. Tables 5 and 7 include data for 75% and 100% load. Analysis has shown that the rms voltage, which includes all the harmonics, produces an inflated value that doesn't represent the torque producing fundamental of the motor; consequently, it cannot be used to estimate the power factor of the motor. On the other hand the power to the motor is a reliable value because of the self-filtering that takes place during digital time averaging, which involves integration of the products of the incremental voltage and current.

Table 4. A 300 V_{dc} performance at 25% and 50% loads controlled by ORNL's sensorless parameter based control scheme

		25% Load											
	MOTOR					INVERTER						SOURCE	
	6-kW 36/30 FSCW SPM		Danfoss VLT 5252 controlled by Aalborg card interfaced to OPAL-RT								Robicon dc supply		
RPM	Torque, N-m	Power, W	v_{an}, V_{rms}	i_a, A_{rms}	v_{bn}, V_{rms}	i_b, A_{rms}	v_{cn}, V_{rms}	i_c, A_{rms}	Power to Motor, W	Measured Loss, W	v_{supply}, V_{dc}	i_{supply}, A_{dc}	Power to inverter, W
450	15.9	749.27	81.3	11.61	81.11	11.35	81.04	11.38	784	34.73	300.58	3.03	873
900	16	1508	98.89	12.94	98.89	12.63	98.7	12.74	1609	101	307.73	5.42	1678
2000	7.2	1508	136.79	17.58	134.3	15.58	138.69	16.55	1742	234	302.44	6.13	1842
3000	4.8	1507.5	146.52	7.46	146.26	7.67	146.28	7.7	1942	434.5	307.7	6.43	1938
4000	3.6	1508	150.1	11.52	144.14	12.61	149.33	12.06	2236	728	307.48	7.28	2262
		50% Load											
	MOTOR					INVERTER						SOURCE	
	6-kW 36/30 FSCW SPM		Danfoss VLT 5252 controlled by Aalborg card interfaced to OPAL-RT								Robicon dc supply		
RPM	Torque, N-m	Power, W	v_{an}, V_{rms}	i_a, A_{rms}	v_{bn}, V_{rms}	i_b, A_{rms}	v_{cn}, V_{rms}	i_c, A_{rms}	Power to Motor, W	Measured Loss, W	v_{supply}, V_{dc}	i_{supply}, A_{dc}	Power to inverter, W
450	31.8	1498.5	81.56	21.39	81.46	21.45	81.58	21.33	1532	33.5	300.71	5.55	1680
900	31.8	2997.1	103.58	21.8	103.48	21.81	103.38	21.87	3073	75.9	300.57	10.84	3264
2000	14.3	2995	135.77	15.58	134.3	16.78	133.34	15.79	3244	249	302.83	10.85	3285
3000	9.5	2985.5	146.32	10.32	146	10.67	146.08	10.31	3390	404.5	307.7	10.96	3384
4000	7.2	3016.7	148.13	13.3	146.82	13.27	148.34	13.18	3687	670.3	307.4	11.99	3709

Table 5. A 300 V_{dc} performance at 75% and 100% loads controlled by ORNL's sensorless parameter based control scheme

		75% Load											
	MOTOR			INVERTER								SOURCE	
6-kW 36/30 FSCW SPM			Danfoss VLT 5252 controlled by Aalborg card interfaced to OPAL-RT								Robicon dc supply		
RPM	Torque, N-m	Power, W	v_{an}, V_{rms}	i_a, A_{rms}	v_{bn}, V_{rms}	i_b, A_{rms}	v_{cn}, V_{rms}	i_c, A_{rms}	Power to Motor, W	Measured Loss, W	v_{supply}, V_{dc}	i_{supply}, A_{dc}	Power to inverter, W
450	47.7	2247.8	85.9	36.2	85.86	35.83	85.79	36.09	2537	289.2	300.78	9.42	2841
900	47.7	4495.6	112.9	32	112.79	31.8	112.91	32.04	4645	149.4	300.5	16.33	4926
2000	21.5	4502.9	138.82	19.8	132.09	18.94	135.83	20.81	4702.9	200	302.74	15.65	4747
3000	14.3	4494	146.07	13.42	146.09	13.44	145.84	13.73	4874	380	307.62	15.97	4877
4000	10.7	4483.1	147.24	15.53	148.5	15.91	146.82	15.76	5096	612	307.4	17	5111
		100% Load											
	MOTOR			INVERTER								SOURCE	
6-kW 36/30 FSCW SPM			Danfoss VLT 5252 controlled by Aalborg card interfaced to OPAL-RT								Robicon dc supply		
RPM	Torque, N-m	Power, W	v_{an}, V_{rms}	i_a, A_{rms}	v_{bn}, V_{rms}	i_b, A_{rms}	v_{cn}, V_{rms}	i_c, A_{rms}	Power to Motor, W	Measured Loss, W	v_{supply}, V_{dc}	i_{supply}, A_{dc}	Power to inverter, W
450	63.7	3001.8	90.86	45.35	90.65	45.17	90.83	45.41	3501	499.2	300.75	12.4	3725
900	63.7	6003.6	120.63	44.73	120.63	44.1	120.74	44.54	6511	507.4	300.26	22.35	6703
2000	28.6	5990	139.62	29.02	137.83	26.8	135.73	29.21	6195	205	302.52	20.82	6315
3000	19.1	6000.4	145.75	18.72	145.9	18.79	146.03	18.68	6327	326.6	307.62	20.59	6362
4000	14.4	6030.4	146.43	19.36	146.25	20.43	149.36	18.63	6571	540.6	307.35	21.42	6612

Table 6. A 250 V_{dc} performance at 25% and 50% loads controlled by ORNL's sensorless parameter based control scheme

	25% Load												
	MOTOR		INVERTER									SOURCE	
	6-kW 36/30 FSCW SPM		Danfoss VLT 5252 controlled by Aalborg card interfaced to OPAL-RT									Robicon dc supply	
RPM	Torque, N-m	Power, W	v_{an}, V_{rms}	i_a, A_{rms}	v_{bn}, V_{rms}	i_b, A_{rms}	v_{cn}, V_{rms}	i_c, A_{rms}	Power to Motor, W	Measured Loss, W	v_{supply}, V_{dc}	i_{supply}, A_{dc}	Power to inverter, W
450													
900	15.9	1498.5	86.93	12.35	86.72	11.99	86.75	12.26	1574	75.5	253.31	6.5	1648
2000	7.2	1507.2	118.44	11.84	118.79	11.13	118.83	12.37	1762	254.8	250.82	7.2	1766
3000	4.8	1508	121.47	11.16	120.94	10.87	121.07	10.19	1899	391	253.11	7.57	1905
4000	3.6	1508	120.65	14.07	125.32	13.48	123.17	13.97	2226	718	253.23	8.8	2228
	50% Load												
	MOTOR		INVERTER									SOURCE	
	6-kW 36/30 FSCW SPM		Danfoss VLT 5252 controlled by Aalborg card interfaced to OPAL-RT									Robicon dc supply	
RPM	Torque, N-m	Power, W	v_{an}, V_{rms}	i_a, A_{rms}	v_{bn}, V_{rms}	i_b, A_{rms}	v_{cn}, V_{rms}	i_c, A_{rms}	Power to Motor, W	Measured Loss, W	v_{supply}, V_{dc}	i_{supply}, A_{dc}	Power to inverter, W
450													
900	31.9	3006.5	94.6	21.81	94.79	21.81	94.6	21.78	3073	66.5	253.35	12.73	3197
2000	14.3	2995	118.26	14.03	118.11	14.21	119.04	15.04	3192	197	250.77	12.89	3203
3000	9.6	3016.9	121.06	12.85	121.11	12.92	120.89	12.98	3318	301.1	253.27	12.97	3401
4000	7.2	3015.9	122.34	15.73	121.32	15.9	124.93	15.48	3634	618.1	253.32	14.47	3651

Table 7. A 250 V$_{dc}$ performance at 75% and 100% loads controlled by ORNL's sensorless parameter based control scheme

		75% Load												
	MOTOR			INVERTER									SOURCE	
6-kW 36/30 FSCW SPM			Danfoss VLT 5252 controlled by Aalborg card interfaced to OPAL-RT									Robicon dc supply		
RPM	Torque, N-m	Power, W	v$_{an}$, V$_{rms}$	i$_a$, A$_{rms}$	v$_{bn}$, V$_{rms}$	i$_b$, A$_{rms}$	v$_{cn}$, V$_{rms}$	i$_c$, A$_{rms}$	Power to Motor, W	Measured Loss, W	v$_{supply}$, V$_{dc}$	i$_{supply}$, A$_{dc}$	Power to inverter, W
450													
900	47.7	4500.6	102.72	31.96	102.52	31.8	102.63	32.03	4688	187.4	253.34	19.24	4865
2000	21.5	4500.7	118.56	19.53	117.84	19.92	117.49	19.9	4690	189.3	250.72	18.76	4739
3000	14.4	4522.4	120.68	16.32	120.86	16.14	120.83	16.01	4868	345.6	253.15	19.09	4903
4000	10.8	4523.9	124.15	17.34	122.6	18.21	121.1	18.58	5122	598.1	253.19	20.4	5138
		100% Load												
	MOTOR			INVERTER									SOURCE	
6-kW 36/30 FSCW SPM			Danfoss VLT 5252 controlled by Aalborg card interfaced to OPAL-RT									Robicon dc supply		
RPM	Torque, N-m	Power, W	v$_{an}$, V$_{rms}$	i$_a$, A$_{rms}$	v$_{bn}$, V$_{rms}$	i$_b$, A$_{rms}$	v$_{cn}$, V$_{rms}$	i$_c$, A$_{rms}$	Power to Motor, W	Measured Loss, W	v$_{supply}$, V$_{dc}$	i$_{supply}$, A$_{dc}$	Power to inverter, W
450													
900	63.7	6010.3	111.96	45.44	112.04	45.01	111.86	45.1	6406	395.7	252.94	26.28	6623
2000	28.7	6010.9	119.77	22.78	119.61	23.47	119.88	24.16	6138	127.1	253.4	24.43	6179
3000	19.1	6000.4	120.65	20.16	120.52	20.01	120.5	21.04	6277	276.6	253.02	25.2	6324
4000	14.4	6031.9	120.76	22.26	123.95	21.15	122.35	22.4	6520	488.1	253.13	26.09	6549

5.0 CONCLUSIONS

- This control system <u>does not require</u> any type of <u>current feedback</u>, although it needs accurate information about dc voltage, motor speed, and rotor position which can be obtained from the same speed feedback sensor.
- Even though a test was carried out at 9 kHz PWM switching frequency, when modulation index approached 1, PWM output became a little bit unstable. Since IO cards are FPGA based, sine triangle PWM can be implemented in the card itself. This will free a lot of CPU time and also PWM outputs will be more stable and reliable.
- The speed at which minimum current, n_{min}, occurs depends linearly on developed power and inversely on the maximum fundamental inverter voltage. The unique speed, n_{min}, varies with voltage leaving room for optimization. If a motor spends a substantial amount of time at a certain speed, such as 60 mph, it could be desirable to choose a dc supply voltage which causes the minimum current at half speed. This would involve using a dc supply larger than the minimum and using control to restrain the torque envelope. It can be verified from Tables 3, 4, 5, and 6 that the current at $n_{min} = 2933$ rpm is the minimum and also inverter losses with 300 V dc supply are minimum at this n_{min}.
- Characteristic motor current, which permits operation at high CPSR, depends solely on machine parameters E_b, Ω_b, and L and is independent of motor load and dc supply voltage. This lowers its efficiency at partial load conditions at higher speeds. Providing voltage higher than necessary to support rated torque at base speed cannot reduce the current at high speed.
- It is advantageous to have the inductance higher than "optimal" because it enables the motor to develop the required power with lower current and attendant efficiency increase.

Control of the voltage lead angle at high speeds allows a PMSM to operate at constant power, but it doesn't assure operation within rated current. Inductance is the critical factor that assures operation within rated current.

APPENDIX A
CALCULATION OF V_D, V_Q, I_D, AND I_Q FOR A PMSM FROM PERFORMANCE MEASUREMENTS ASSUMING V_{RMS}, I_{RMS}, ACTIVE POWER, ANGULAR SPEED, AND MOTOR PARAMETERS ARE KNOWN

Comparison of ORNL's sensorless simple parameter based (SSPB) control with vector control requires an estimate of the dc, which is that part of the stator current that weakens the magnetic flux of the magnets so that the motor may reach higher speeds. Such an estimate depends on an accurate knowledge of the motor parameters, resistance and inductance, and accurate measurements of rms voltage, rms current, active power, and angular velocity. Measurements from the motor performance matrix yielded estimates of power factor that were much lower than expected from the excellent performance measurements. The measured value for active power is dependable because integration of the product of current and voltage, which have different harmonics, is digitally integrated. This integration removes the harmonics leaving an integral of the power delivered at the fundamental frequency. The power factor is estimated by the quotient of the active power to the product of the rms voltage and rms current. The rms voltage has many harmonics from the PWM voltage control. In the calculation of the rms voltage, each of these is squared and added allowing no opportunity to filter the harmonics. The result is that the rms voltage is inflated. The harmonic content of the rms current is much less than that of the rms voltage, but it too can be inflated. Appendices A and B provide two methods to estimate the dc. The equations in Appendix A may be useful in the future, when a method is used to directly and accurately measure the power factor by filtering the harmonics before they are sampled by the digital scope. Application to the measurement data taken during evaluation of the SSPB control scheme gave meaningless estimates of the dc because of the poor estimates of power factor.

A.1. THREE-PHASE CURRENT AND VOLTAGE IN A LABORATORY REFERENCE FRAME

An elegant and useful approach to developing the steady-state design equations for a synchronous PM motor is to transform the stator variables, current, voltage, and power from a three-phase stationery-coordinate reference frame into a new rotating reference frame. The new reference frame will rotate synchronously with the electrical frequency, which will cause the currents and voltages to be constant as shown below. The transformation was introduced by Blondel [7], Doherty and Nickle [8], and Park [9].

In a stationary coordinate system which is fixed in the stator, the most general currents and voltages are expressed as

$$
\begin{aligned}
i_a &= i_a^{pk} \cos(\omega_{el} t - \varepsilon_a) & v_a &= v_a^{pk} \cos(\omega_{el} t - \alpha_a) \\
i_b &= i_b^{pk} \cos\left(\omega_{el} t - \varepsilon_b - \frac{2\pi}{3}\right) \text{ and } v_b &= v_b^{pk} \cos\left(\omega_{el} t - \alpha_b - \frac{2\pi}{3}\right). \\
i_c &= i_c^{pk} \cos\left(\omega_{el} t - \varepsilon_c + \frac{2\pi}{3}\right) & v_c &= v_c^{pk} \cos\left(\omega_{el} t - \alpha_c + \frac{2\pi}{3}\right)
\end{aligned}
\tag{A1}
$$

For a balanced system $i_a^{pk} = i_b^{pk} = i_c^{pk} = i^{pk}$ are the peak values for the time-domain current waveform, $v_a^{pk} = v_b^{pk} = v_c^{pk} = v^{pk}$ are the peak values for the time-domain voltage waveform, and $\varepsilon_a = \varepsilon_b, = \varepsilon_c = \varepsilon$ and $\alpha_a = \alpha_b = \alpha_c = \alpha$ are the angles by which the current and voltage, respectively, are shifted counter clockwise with respect to the x'-axis chosen to be the d-axis in a synchronously rotating coordinate system.

In the stationary reference frame, the instantaneous values of i_a, i_b, i_c and v_a, v_b, and v_c can be resolved along the x- and y-axes and viewed as two vectors, $\boldsymbol{i}^{pk}$ and $\boldsymbol{v}^{pk}$, rotating clockwise at angular speed, ω_{el}. By changing the frame of reference to one rotating clockwise synchronously at angular speed, ω_{el}, the projection of the $\boldsymbol{i}^{pk}$ and $\boldsymbol{v}^{pk}$ vectors over the rotating x- and y-axes will remain constant with time. This means that they are dcs and voltages. The behavior just described is shown mathematically by the following equations. The sum of the projections of the instantaneous values of the three phases on the stationary x- and y-axes are

$$i_x = i_a - \frac{i_b}{2} - \frac{i_c}{2} = \frac{3}{2} i^{pk} \cos(\omega_{el}t - \varepsilon),$$

and   (A2)

$$i_y = -i_b \frac{\sqrt{3}}{2} + i_c \frac{\sqrt{3}}{2} = -\frac{3}{2} i^{pk} \sin(\omega_{el}t - \varepsilon).$$

The final terms of Eq. (A2) employ Eq. (A1) and assume that the system is balanced. The two terms are components of the vector, $\boldsymbol{i}^{pk}$. Because of the negative sin term, the tip of the vector traces a clockwise circle a time increases.

A.2. TRANSFORMATION OF BALANCED THREE-PHASE CURRENT AND VOLTAGE TO A SYNCHRONOUSLY ROTATING REFERENCE FRAME

Using the convention that positive rotation, θ, is counterclockwise; the instantaneous coordinates of Eq. (A2) are transformed to a coordinate system rotated by angle, θ, using the transformation matrix

$$\begin{vmatrix} I_{x'} \\ I_{y'} \end{vmatrix} = \begin{vmatrix} \cos(\theta) & \sin(\theta) \\ -\sin(\theta) & \cos(\theta) \end{vmatrix} \begin{vmatrix} i_x \\ i_y \end{vmatrix}.$$ (A3)

From Eq. (A2) and the transformation matrix of Eq. (A3), the new x'- and y'-coordinates are

$$I_{x'} = i_a \cos(\theta) + i_b \cos\left(\theta + \frac{2\pi}{3}\right) + i_c \cos\left(\theta - \frac{2\pi}{3}\right),$$

and   (A4)

$$I_{y'} = -i_a \sin(\theta) - i_b \sin\left(\theta + \frac{2\pi}{3}\right) - i_c \sin\left(\theta - \frac{2\pi}{3}\right).$$

Then substituting Eq. (A1) into Eq. (A4) and employing the trigonometric identities

$$\cos(M)\cos(N) = \frac{1}{2}\left[\cos(M+N) + \cos(M-N)\right],$$ (A5)

and

42

$$\cos(M)\sin(N) = \frac{1}{2}[\sin(M+N) - \sin(M-N)], \tag{A6}$$

we find that

$$I_{x'} = \frac{3}{2}i^{pk}\cos(\theta + \omega t - \varepsilon), \tag{A7}$$

and

$$I_{y'} = -\frac{3}{2}i^{pk}\sin(\theta + \omega t - \varepsilon). \tag{A8}$$

If the angle θ is chosen as $\theta = -\omega t$, then the rotating frame is synchronous with the electrical frequency. Since the convention is that the d-axis corresponds to the x'-axis and the q-axis corresponds to the y'-axis, the two currents from Eqs. (A7) and (A8) become the time-independent equations

$$I_d = \frac{3}{2}i^{pk}\cos(\varepsilon), \tag{A9}$$

and

$$I_q = \frac{3}{2}i^{pk}\sin(\varepsilon). \tag{A10}$$

Equations (A9) and (A10) combine to give the total current, which is

$$I^{pk} = \sqrt{I_{x'}^2 + I_{y'}^2} = \frac{3}{2}i^{pk}. \tag{A11}$$

A similar set of Eqs. (A9–A11) exist for voltage where I is replaced by V and ε is replaced by α.

For the synchronous reference frame with its d-axis rotated clockwise, $\omega_{el}t$ radians the angle of the current subtracts ε radians from $\omega_{el}t$ and the angle of the voltage subtracts α radians from $\omega_{el}t$. This is illustrated in Fig. A1 which shows the synchronous frame with its phasor quantities.
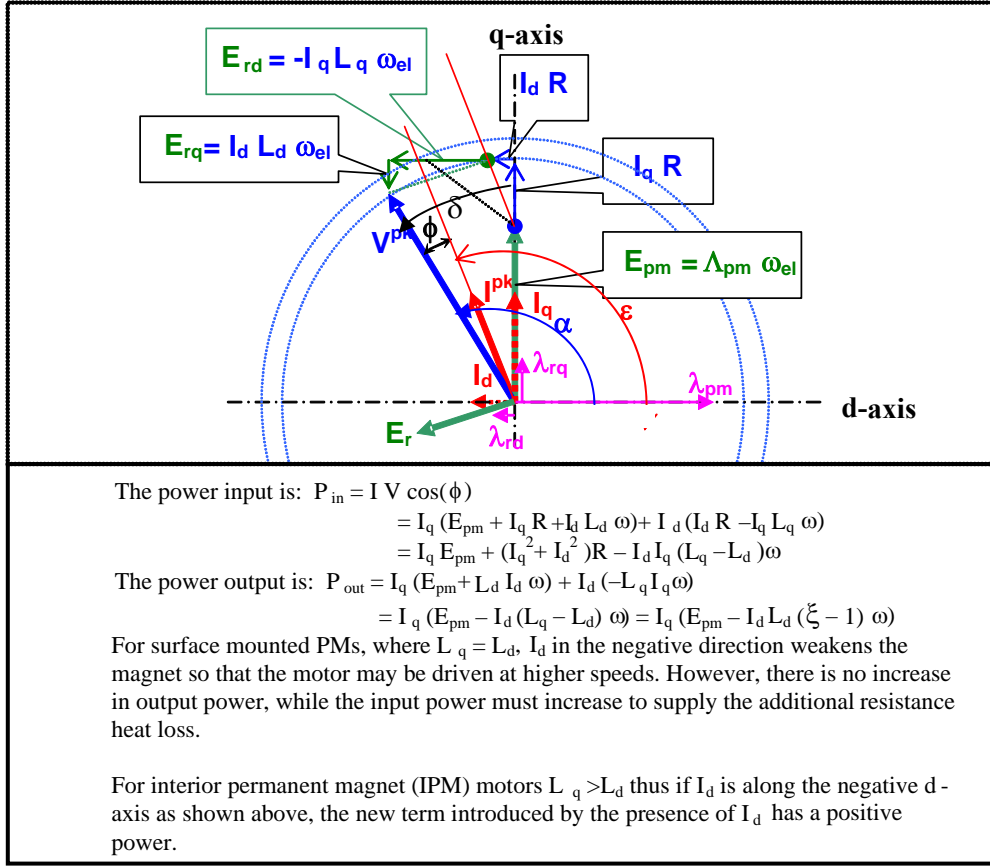
Fig. A1. Phasor representation of the synchronous reference frame of a PM motor.

The contents of the figure box:

$E_{rd} = -I_q L_q \omega_{el}$

$E_{rq} = I_d L_d \omega_{el}$

$!I_d R$

$I_q R$

q-axis

δ

ϕ

V^{pk}

$E_{pm} = \Lambda_{pm} \omega_{el}$

I^{pk}

I_q

α

ε

I_d

λ_{rq}

λ_{pm}

E_r

λ_{rd}

d-axis

The power input is: $P_{in} = I \, V \cos(\phi)$
$$= I_q \, (E_{pm} + I_q \, R + I_d \, L_d \, \omega) + I_d \, (I_d \, R - I_q \, L_q \, \omega)$$
$$= I_q \, E_{pm} + (I_q^2 + I_d^2) R - I_d \, I_q \, (L_q - L_d) \omega$$

The power output is: $P_{out} = I_q \, (E_{pm} + L_d \, I_d \, \omega) + I_d \, (-L_q \, I_q \, \omega)$
$$= I_q \, (E_{pm} - I_d \, (L_q - L_d) \, \omega) = I_q \, (E_{pm} - I_d \, L_d \, (\xi - 1) \, \omega)$$

For surface mounted PMs, where $L_q = L_d$, I_d in the negative direction weakens the magnet so that the motor may be driven at higher speeds. However, there is no increase in output power, while the input power must increase to supply the additional resistance heat loss.

For interior permanent magnet (IPM) motors $L_q > L_d$ thus if I_d is along the negative d-axis as shown above, the new term introduced by the presence of I_d has a positive power.

A.3. VECTOR EQUATIONS IN A SYNCHRONOUS REFERENCE FRAME TO DETERMINE THE VOLTAGE AND PHASE ANGLE

From the Phasor diagram of Fig. A1, two equations may be established to calculate the value of ε from which all other quantities may be determined. The first equation is

$$V^{pk} \cos(\phi + \varepsilon) = -\omega_{el} L_q I^{pk} \sin \varepsilon + R I^{pk} \cos \varepsilon, \tag{A12}$$

and the second is

$$V^{pk} \sin(\phi + \varepsilon) = R I^{pk} \sin \varepsilon + \omega_{el} L_d I^{pk} \cos \varepsilon + \Lambda_{pm} \omega_{el}. \tag{A13}$$

Expanding the sin and cos terms in Eqs. (A12) and (A13) and substituting the transformation relation between I^{pk} and i^{pk} in Eq. (A11) and its companion voltage relations, V^{pk} and v^{pk}, and back-emf relations, E^{pk} and e^{pk}, along with the equalities that relate sinusoidal peak and rms quantities, $i^{pk} = \sqrt{2} i_{rms}$ and $v^{pk} = \sqrt{2} v_{rms}$, leads to the simultaneous linear equations in *cos* ε and *sin* ε

$$\left[\frac{3}{2}\sqrt{2}v_{rms}\,cos\,\phi-R\frac{3}{2}\sqrt{2}i_{rms}\right]cos\,\varepsilon-\left[\frac{3}{2}\sqrt{2}v_{rms}\,sin\,\phi-\omega_{el}L_q\frac{3}{2}\sqrt{2}i_{rms}\right]sin\,\varepsilon=0\,, \qquad \text{(A14)}$$

and

$$\left[\frac{3}{2}\sqrt{2}v_{rms}\,sin\,\phi-\omega_{el}L_d\frac{3}{2}\sqrt{2}i_{rms}\right]cos\,\varepsilon+\left[\frac{3}{2}\sqrt{2}v_{rms}\,cos\,\phi-R\frac{3}{2}\sqrt{2}i_{rms}\right]sin\,\varepsilon=$$
$$\frac{3}{2}\sqrt{2}k_v\Omega_{rpm} \qquad \text{(A15)}$$

A.4. RELATIONS BETWEEN PHASE ANGLES IN A SYNCHRONOUS REFERENCE FRAME AND PERFORMANCE TEST MEASUREMENTS

The solutions are

$$cos(\varepsilon)=\frac{k_v\Omega_{rms}^{rpm}\left[v_{rms}\,sin\phi-\omega_{el}L_q i_{rms}\right]}{v_{rms}^2+R^2 i_{rms}^2-2v_{rms}i_{rms}\left[\omega_{el}\dfrac{(L_q+L_d)}{2}sin\phi+Rcos\phi\right]+\omega_{el}^2 L_q L_d i_{rms}^2}\,, \qquad \text{(A16)}$$

and

$$sin(\varepsilon)=\frac{k_v\Omega_{rms}^{rpm}\left[v_{rms}\,cos\phi-Ri_{rms}\right]}{v_{rms}^2+R^2 i_{rms}^2-2v_{rms}i_{rms}\left[\omega_{el}\dfrac{(L_q+L_d)}{2}sin\phi+Rcos\phi\right]+\omega_{el}^2 L_q L_d i_{rms}^2}\,. \qquad \text{(A17)}$$

The sign of $cos(\varepsilon)$ in Eq. (A16) distinguishes between values of positive and negative values of the dc, which is negative when it weakens the magnet flux. For negative i_d, ε is greater than 90°.

Once ε is known the remaining quantities in the synchronous frame may be calculated as

$$\alpha=\phi+\varepsilon\,, \qquad \text{(A18)}$$

$$\delta=\alpha-\frac{\pi}{2}\,, \qquad \text{(A19)}$$

$$I_d=\frac{3}{2}\sqrt{2}i_{rms}\,cos\,\varepsilon\,, \qquad \text{(A20)}$$

$$I_q=\frac{3}{2}\sqrt{2}i_{rms}\,sin\,\varepsilon\,, \qquad \text{(A21)}$$

$$V_d=\frac{3}{2}\sqrt{2}v_{rms}\,cos\,\alpha\,, \qquad \text{(A22)}$$

45

$$V_q = \frac{3}{2}\sqrt{2}v_{rms}\ sin\ \alpha,$$ (A23)

and

$$E_{pm} = \frac{3}{2}\sqrt{2}k_v\Omega_{rms}^{rpm}.$$ (A24)

The value of δ is the control angle in the SSPB control scheme. These equations are in terms of the measured rms current, i_{rms}, rms voltage, v_{rms}, the phase angle between the voltage and current, ϕ, and the motor parameters resistance, R, quadrature phase inductance, L_q, direct phase inductance, L_d, and electrical frequency, ω_{el}.

APPENDIX B
CALCULATION OF THE SPEED, N_{MIN}, AT WHICH THE
CURRENT MAGNITUDE IS MINIMUM

Equations (17) and (19) of the report enable one to calculate the relative speed at which the current magnitude is a minimum. The equations are restated here for convenience as

$$sin\ \delta = \frac{X_b P}{3V_{max} E_b}\ ,\tag{17}$$

and

$$n_{min} = \frac{V_{max}}{E_b\ cos\ \delta}\ .\tag{19}$$

When Eq. (19) is substituted into Eq. (18) for the minimum current, the result is

$$I_{min} = \frac{\sqrt{V_{max}^2 - 2n_{min}V_{max}E_b\ cos\ \delta + n_{min}^2 E_b^2}}{n_{min}X_b} = \frac{E_b\ sin\ \delta}{X_b} = \frac{P}{3V_{max}}\ ,\tag{20}$$

which shows that the minimum current is independent of the motor parameters and depends linearly on the power and inversely on the maximum fundamental inverter voltage. Table B.1 summarizes the minimum speeds and currents for the four power levels measured. As a useful summary

$$n_{min} = \frac{N_{min}}{N_{base}}\ ,$$

N_{base} = 900 rpm,

E_{base} = 49.45 V_{rms},

$$\omega_{base}^{el} = \frac{N_{base}2\pi 15}{60} = 1413.7\ \text{rad/s},$$

$L = 0.0013$ henries,

$$X_b = \omega_{base}^{el}L = 1.838\ \text{ohms, and}$$

$$V_{max} = \frac{\sqrt{2}}{\pi}V_{dc} = 0.450V_{dc}\ ,\ \text{rms volts.}$$

Table B.1. Calculation of minimum current and the speed at which it occurs

Power, watts	V_{dc} = 300 V_{dc} V_{max} = 135 V_{rms}			V_{dc} = 250 V_{dc} V_{max} = 112.5 V_{rms}		
	δ, degrees	N_{min}, rpm	I_{min}, A_{rms}	δ, degrees	N_{min}, rpm	I_{min}, A_{rms}
1500	7.90	2481	3.70	9.50	2076	4.44
3000	15.97	2556	7.40	19.28	2169	8.88
4500	24.38	2698	11.10	29.69	2357	13.33
6000	33.39	2943	14.81	41.34	2728	17.77

APPENDIX C
CALCULATION OF I_D FOR A PMSM FROM PERFORMANCE MEASUREMENTS ASSUMING I_{RMS}, SHAFT POWER, AND ANGULAR SPEED ARE KNOWN

Since the current has less harmonic content than the voltage, a better estimate of the dc can be expected if one uses the relation between mechanical shaft power and the real current, $P_{shaft} = 3I_r nE_b$, which leads

to $I_r = \dfrac{P_{shaft}}{3nE_b}$. The dc is then calculated from the measured rms current using the

relation $I_d = \sqrt{I_{rms}^2 - I_r^2}$. The angle between the total current and the back-emf, which is the shaft power

factor, is given by the relation $\theta_{shaft} = tan^{-1}\dfrac{I_d}{I_r}$. For speeds below base speed such as 450 rpm, the value

of θ is negative. For speeds above base speed the value of θ is positive. Calculated values are shown in Table C.1.

Table C.1. Calculation of dc (field weakening) and shaft power factor

E_{base}=	49.45	volts					
		Measured Data			Calculated Data		
RPM	Relative speed, n	Shaft Power, kW	Irms Avg	Ir = Iq	Ix = Id	Shaft Power Factor Angle, degrees	Load
450	0.5	749	11.45	10.10	5.39	-28.09	25%
450	0.5	1499	21.39	20.20	7.03	-19.18	50%
450	0.5	2248	36.04	30.30	19.51	-32.77	75%
450	0.5	3002	45.31	40.47	20.38	-26.73	100%
900	1	1508	12.77	10.17	7.73	37.25	25%
900	1	2997	21.83	20.20	8.27	22.26	50%
900	1	4496	31.95	30.30	10.12	18.47	75%
900	1	6004	44.46	40.47	18.41	24.46	100%
2000	2.222	1508	16.57	4.57	15.93	73.97	25%
2000	2.222	2995	16.05	9.08	13.23	55.53	50%
2000	2.222	4503	19.85	13.66	14.40	46.52	75%
2000	2.222	5990	28.34	18.17	21.75	50.12	100%
3000	3.333	1508	7.61	3.05	6.97	66.38	25%
3000	3.333	2986	10.43	6.04	8.50	54.63	50%
3000	3.333	4494	13.53	9.09	10.02	47.80	75%
3000	3.333	6000	18.73	12.13	14.27	49.62	100%
4000	4.444	1508	12.063	2.29	11.84	79.07	25%
4000	4.444	3017	13.25	4.58	12.43	69.80	50%
4000	4.444	4483	15.73	6.80	14.18	64.39	75%
4000	4.444	6030	19.47	9.15	17.19	61.98	100%

6.0 REFERENCES

[1] A. M. El-Refaie and T. M. Jahns, "Optimal Flux Weakening in Surface PM Machines using Fractional-Slot Concentrated Windings," pp.790–800 in *IEEE Trans. Industry Applications,* **41**(3), May–June, 2005.

[2] A. M. El-Refaie, T. M. Jahns, P. J. McCleer, and J. W. McKeever, "Experimental Verification of Optimal Flux Weakening in Surface PM Machines Using Concentrated Windings," *Conf. Rec. IEEE Industry Applications Society Annual Meeting*, Hong Kong, October 2–6, 2005.

[3] A. M. El-Refaie and T. M. Jahns, "Optimal Flux Weakening in Surface PM Machines using Concentrated Windings," pp. 1038–1047 in *Conf. Recl IEEE Industry Applications Society Annual Meeting,* **2**, Seattle, Washington, October 2004.

[4] J. S. Lawler, J. M. Bailey, J. W. McKeever, and J. Pinto, "Extending the Constant Power Speed Range of the Brushless DC Motor through Dual Mode Inverter Control," pp. 783–793 in *IEEE Trans. Power Electron.*, 19(3), May 2004.

[5] J. S. Lawler, J. M. Bailey, J. W. McKeever, and J. Pinto, "Limitations of the CPA Method for Constant Power Operation of the Brushless DC Motor," pp. 174–180 in *Proc. IEEE Southeast Conf.*, April 2002.

[6] P. B. Reddy and T. M. Jahns, *Final Report on Control Algorithm to Improve the Partial Load Efficiency of Surface PM Machines with Fractional Slot Concentrated Windings*, ORNL/TM-2007/048, Oak Ridge National Laboratory, UT-Battelle, Oak Ridge, Tennessee, April 2007.

[7] O. I. Elgerd, *Electric Energy Systems Theory: Introduction*, McGraw-Hill Book Company, Chapter 4, 1971.

[8] R. E. Doherty and C. A. Nickle, "Synchronous Machines," pp. 912–942 in *AIEE Trans.*, **45**, 1926.

[9] R. H. Park, "Two Reaction Theory of Synchronous Machines – Generalized Method of Analysis," pp. 716–727 in *AIEE Trans.*, **48**, 1929.

DISTRIBUTION

Internal

1. D. J. Adams
2. K. P. Gambrell
3. E. C. Fox
4. L. D. Marlino
5. J. W. McKeever
6. M. Olszewski
7. N. Patil
8. Laboratory Records

External

9. R. Al-Attar, DCX, raa9@dcx.com.
10. T. Q. Duong, U.S. Department of Energy, EE-2G/Forrestal Building, 1000 Independence Avenue, S.W., Washington, D.C. 20585.
11. R. R. Fessler, BIZTEK Consulting, Inc., 820 Roslyn Place, Evanston, Illinois 60201-1724.
12. G. Hagey, Sentech, Inc., 501 Randolph St., Williamsburg, Virginia 23185.
13. E. Jih, Ford Motor Company, Scientific Research Laboratory, 2101 Village Road, MD-1170, Rm. 2331, Dearborn, Michigan 48121.
14. K. J. Kelly, National Renewable Energy Laboratory, 1617 Cole Boulevard, Golden, Colorado 80401
15. J. S. Lawler, University of Tennessee, Department of Electrical and Computer Engineering, 402 Ferris Hall, Knoxville, Tennessee 37996-2100.
16. A. Lee, Daimler Chrysler, CIMS 484-08-06, 800 Chrysler Drive, Auburn Hills, Michigan 48326-2757.
17. F. Leonardi, Ford Motor Company, 15050 Commerce Drive, North, Dearborn, Michigan 48120-1261.
18. F. Liang, Ford Motor Company, Scientific Research Laboratory, 2101 Village Road, MD1170, Rm. 2331/SRL, Dearborn, Michigan 48121.
19. M. W. Lloyd, Energetics, Inc., 7164 Columbia Gateway Drive, Columbia, Maryland 21046.
20. J. Maquire, General Motors Advanced Technology Center, 3050 Lomita Boulevard, Torrance, California 90505.
21. M. Mehall, Ford Motor Company, Scientific Research Laboratory, 2101 Village Road, MD-2247, Rm. 3317, Dearborn, Michigan 48124-2053.
22. Jean A. Montemarano–Naval Surface Warfare Center, Carderock Division; Code 642, NSWCD, 9500 MacArthur Boulevard; West Bethesda, Maryland 20817
23. N. Olds, United States Council for Automotive Research (USCAR), nolds@uscar.org.
24. J. Rogers, Chemical and Environmental Sciences Laboratory, GM R&D Center, 30500 Mound Road, Warren, Michigan 48090-9055.
25. S. A. Rogers, U.S. Department of Energy, EE-2G/Forrestal Building, 1000 Independence Avenue, S.W., Washington, D.C. 20585.
26. G. S. Smith, General Motors Advanced Technology Center, 3050 Lomita Boulevard, Torrance, California 90505.
27. E. J. Wall, U.S. Department of Energy, EE-2G/Forrestal Building, 1000 Independence Avenue, S.W., Washington, D.C. 20585.
28. B. Welchko, General Motors Advanced Technology Center, 3050 Lomita Boulevard, Torrance, California 90505.
29. P. G. Yoshida, U.S. Department of Energy, EE-2G/Forrestal Building, 1000 Independence Avenue, S.W., Washington, D.C. 20585.